Gabor Mode Enrichment in Large Eddy Simulations of Turbulent Flow

A. S. Ghate[1] and S. K. Lele[1,2]†

[1]Department of Aeronautics & Astronautics, Stanford University, Stanford, CA
[2]Department of Mechanical Engineering, Stanford University, Stanford, CA

(Received xx; revised xx; accepted xx)

A turbulence enrichment model for subfilter-scale motions in Large Eddy Simulations (LES) is comprehensively evaluated in the context of *a-posteriori* analysis. The paper further develops the Gabor mode enrichment model first introduced in Ghate & Lele (2017) by analysing three key requisites of LES enrichment using solenoidal small scale-velocity fields: a) consistent spectral extrapolation and improvement of resolved single- and two-point second order correlations, b) ability to accurately capture the flow physics responsible for temporal decorrelation at small scales, and c) accurate representation of spatially localized and intermittent inter-scale energy transfer between scales resolved by the coarse grid LES and subfilter scales. We argue that the spatially and spectrally localized Gabor wavepackets offer an optimal basis to represent small scale turbulence within quasi-homogeneous regions, although the alignment of fine scale vorticity alignment with large scale strain appears to be somewhat overemphasized. Consequently, we interpret the resulting subfilter scales as those induced by a set of spatially dispersed Burgers-Townsend vortices with orientations determined by the larger scale velocity gradients resolved by the coarse grid LES. Enrichment of coarse grid simulations of two high Reynolds number flow configurations, homogeneous isotropic turbulence and a rough-wall turbulent boundary layer, show promising results.

Key words:

1. Introduction

It is now widely appreciated that turbulence closures based on Reynolds averaging have limited capabilities and as noted by Spalart (2015), methods that at least resolve the dynamics of largest energy containing, and geometry influenced eddies are naturally suited for a much broader range of engineering applications. Large Eddy Simulations employing a suitable wall-stress closure (wall-model) are among the most accurate methodologies to capture a wide range of turbulent physics including smooth body separation, unsteady wall-pressure and heat-transfer effects. As detailed in recent reviews by Larsson *et al.* (2016) and Bose & Park (2018), wall modeling in LES has come a long way since the first algebraic stress models developed by Deardorff (1970), Schumann (1975) and subsequent inviscid rough-surface adaptation by Moeng (1984) using Monin-Obukhov theory. In engineering applications, wall models based on equilibrium and non-equilibrium assumptions applied to thin boundary layer equations have been deployed with reasonable success to predict skin friction and wall-pressure in complex flow configurations at very

† Email address for correspondence: lele@stanford.edu

high Reynolds numbers (Piomelli & Balaras 2002; Kawai & Larsson 2012; Kawai & Asada 2013).

These recent successes of LES lead to a natural follow up question. While LES is by design meant to provide improved accuracy of moments (ensemble/statistical averages of flow variables) by explicitly resolving the geometry dependent dynamics of the largest scales of motion and modeling the effect of smaller scales, it is only capable of providing dynamical description of turbulence with a limited spatio-temporal bandwidth. This is particularly true in canonical wall turbulence since the integral length scales vary roughly linearly with distance from the wall (Jiménez 2012). In regions above the buffer layer where the effect of the viscous boundary condition is of diminishing significance, a wall-modelled Large Eddy Simulation (WMLES) can only barely capture the integral length scale of the flow, thereby severely limiting the resolvable turbulent kinetic energy. This aspect of under-resolution can easily be acknowledged by considering geophysical flows where WMLES of planetary boundary layers at $Re_\tau \approx 10^6 - 10^7$ (Smits *et al.* 2011) are typically done using only $\mathcal{O}(10^6 - 10^9)$ total grid points (Jiang *et al.* 2018; Brasseur & Wei 2010) depending on the application. Turbulence enrichment, where the geometry/boundary influence large scales are solved using conventional LES and subfilter scales are synthesized, is a natural solution that can potentially enable broadband representation of turbulence at low cost in several applications including wind energy and external hydro- and aerodynamics which deal with wall-pressure induced unsteady structural vibration and noise generation. Recent work in particle-laden turbulence (Mazzitelli *et al.* 2014; Bassenne *et al.* 2019) also underscores the need for synthesis of scales subfilter to the LES of the carrier (fluid) phase. The enrichment model introduced in Ghate & Lele (2017) tackled this aspect of LES directly via representation of small scale turbulence using *Fourier-Gabor modes* together with systematic physics based modeling of the equation governing subfilter-scale flow in the context of Planetary Boundary Layer turbulence in an *a-priori* setting where the large scales were represented by spatial filtering of high resolution DNS or LES data. In this paper we significantly extend that approach for use in a-posteriori LES.

The primary requisites of a basic turbulence enrichment are systematically introduced in Section 2. In Section 3, the notion of a spatially and spectrally localized *Gabor mode/wavepacket* is introduced and by appealing to the assumption of *quasi-homogeneity* of subfilter scales, we argue that these modes form an optimal numerical basis to statistically represent small-scale turbulence, and for its temporal evolution. Sections 4 and 5 comprehensively investigate the a-posteriori enrichment of coarse-grid simulations of isotropic turbulence and rough-wall turbulent channel flow and identify the key strengths of the proposed model. The computational cost of the approach and salient implementation details are included in an Appendix. Summarizing remarks made in Section 6 are used to conclude the paper.

2. Preliminary background on turbulence enrichment

Inspired by a *thought problem* introduced by Wyngaard (2010) to introduce Large Eddy Simulation (LES), we first introduce the notion of small scale enrichment by considering temporally stationary turbulence where *resolved* and *subfilter* are defined via a spectrally sharp filter (applied in cartesian coordinates) and denoted with superscripts (r) and (s)

respectively. Consider the incompressible, constant density Navier-Stokes equation for the total velocity field, u_i

$$u_i(\boldsymbol{x},t) = u_i^r(\boldsymbol{x},t) + u_i^s(\boldsymbol{x},t) \tag{2.1}$$

where u_i^r is the spatially filtered (resolved) component of u_i.

$$u_i^r(\boldsymbol{x},t) = \int_{\boldsymbol{x'}\in\mathcal{R}^3} u_i(\boldsymbol{x'},t) G_\Delta(\boldsymbol{x'}-\boldsymbol{x}) d\boldsymbol{x'} \tag{2.2}$$

Note that the filter kernel, G_Δ represents a filter applied at Δ scale which is assumed to be spatially constant throughout this work in order to enable commutation with differentiation operators. We have,

$$\partial_t u_i + \partial_j \left(u_i u_j\right) = -\partial_i p + \frac{1}{\mathrm{Re}} \partial_j \partial_j u_i + \beta_i \quad ; \quad \partial_j u_j = 0 \tag{2.3}$$

where the notation, ∂_t is used to denote partial derivative in time, and ∂_i is the spatial partial derivative, β_i is the additional acceleration vector needed to balance dissipation and maintain a statistically stationary state in time.

$$\partial_t u_i^r + \partial_j \left(u_i u_j\right)^r = -\partial_i p^r + \frac{1}{\mathrm{Re}} \partial_j \partial_j u_i^r + \beta_i \quad ; \quad \partial_j u_j^r = 0 \tag{2.4}$$

$$\partial_t u_i^s + \partial_j \left(u_i u_j\right)^s = -\partial_i p^s + \frac{1}{\mathrm{Re}} \partial_j \partial_j u_i^s \quad ; \quad \partial_j u_j^s = 0 \tag{2.5}$$

where we have assumed that the forcing applied is exclusively at superfilter ($\beta = \beta^r$) scales. Further, note that the terminology $(u_i u_j)^r$ corresponds to the spatially filtered tensor field, $(u_i u_j)$ and is typically expressed as $(u_i u_j)^r = u_i^r u_j^r + \tau_{ij}$. Here, $\tau_{ij} = (u_i u_j)^r - u_i^r u_j^r$ is the *residual* stress tensor that is the only unclosed term which is modeled in the equations governing large scales 2.4. The goal of subfilter scale enrichment as defined in this work is generation of small scales with accurate second order space-time correlations of the type:

$$c_{ij}(\boldsymbol{x},t,\boldsymbol{x'},\delta_t) = \left\langle u_i^s(\boldsymbol{x},t) u_j^s(\boldsymbol{x'},t+\delta_t) \right\rangle \tag{2.6}$$

We will separate the discussion into two parts: a) energetics of u_i^s, and b) the temporal problem which is particularly relevant since the scale splitting and filtering procedure is explicitly defined in space and not in time (Eq. 2.2).

2.1. *Interscale energetics*

For a spectrally sharp filter, using Parseval's theorem (which gives $\langle u_i^r u_i^s \rangle = 0$) we see that the mean kinetic energy can be decomposed as

$$\langle u_i u_i \rangle = \langle u_i^r u_i^r \rangle + \langle u_i^s u_i^s \rangle \tag{2.7}$$

Since we are interested in the dynamics of the small scales, we can further expand Equation 2.5 as

$$\partial_t u_i^s + u_j^r \partial_j u_i^s + u_j^s \partial_j u_i^r + u_j^s \partial_j u_i^s = -\partial_i p^s + \frac{1}{\mathrm{Re}} \partial_j \partial_j u_i^s + \partial_j \tau_{ij} \quad ; \quad \partial_j u_j^s = 0 \tag{2.8}$$

The equations that govern the kinetic energy split (Equation 2.7) for homogeneous turbulence are given as:

$$\partial_t \left\langle \frac{u_i u_i}{2} \right\rangle = \langle \beta_i u_i \rangle - \varepsilon = \langle \beta_i u_i^r \rangle - \varepsilon \tag{2.9}$$

$$\partial_t \left\langle \frac{u_i^r u_i^r}{2} \right\rangle = \langle \beta_i u_i^r \rangle + \langle \tau_{ij} \partial_j u_i^r \rangle - \varepsilon_r \tag{2.10}$$

$$\partial_t \left\langle \frac{u_i^s u_i^s}{2} \right\rangle = \left[-\langle u_i^s u_j^s \partial_j u_i^r \rangle - (\langle \tau_{ij} \partial_j u_i^s \rangle) \right] - \varepsilon_s \tag{2.11}$$

where $\varepsilon \approx \varepsilon_s = (1/Re)(\partial_j u_i^s)(\partial_j u_i^s)$ (as $Re \to \infty$, fixed filter width) is the dissipation rate. The term, $\langle \tau_{ij} \partial_j u_i^r \rangle$ in Equation 2.10 can be further simplified as

$$\langle \tau_{ij} \partial_j u_i^r \rangle = -\langle u_i^r \partial_j \tau_{ij} \rangle = -\langle u_i^r \partial_j \left(u_i u_j\right)^r \rangle = -\langle u_i^r \partial_j \left[(u_i u_j) - (u_i u_j)^s \right] \rangle = -\langle u_i^r \partial_j \left(u_i u_j\right) \rangle \tag{2.12}$$

Expanding $(u_i u_j) = ((u_i^r + u_i^s))\left((u_j^r + u_j^s)\right)$ in the last term and simplifying, we obtain the definition for $\langle \tau_{ij} \partial_j u_i^r \rangle$

$$\langle \tau_{ij} \partial_j u_i^r \rangle = -\left\langle u_i^r u_j^r \partial_j u_i^s \right\rangle + \left\langle u_i^s u_j^s \partial_j u_i^r \right\rangle = \langle \tau_{ij} \partial_j u_i^s \rangle + \left\langle u_i^s u_j^s \partial_j u_i^r \right\rangle \tag{2.13}$$

where the second equality follows by simply substituting the definition of τ_{ij} and applying Parseval's theorem. Further note that the right hand side term is exactly the first two terms in Equation 2.11 but with opposite sign. Following Wyngaard (2010), the global (reversible) interscale energy transfer for homogeneous turbulence can be defined as

$$\mathcal{I} = \underbrace{\left[-\left\langle u_i^s u_j^s S_{ij}^r \right\rangle \right]}_{\mathcal{I}_1} + \underbrace{\left[-\left\langle \tau_{ij} S_{ij}^s \right\rangle \right]}_{\mathcal{I}_2} \tag{2.14}$$

where S_{ij} is the symmetric strain rate tensor.

We see that the interscale energy transfer between the large and small scales is due to two distinct mechanisms: 1) work done by subfilter scale stresses against large scale strain ($\mathcal{I}_1$), and 2) work done by residual/subgrid stress against small scale strain ($\mathcal{I}_2$). The definition above must strictly be interpreted as a global balance since it does not hold in a pointwise sense. While the second term in Equation 2.14 can be further simplified as $\left\langle \tau_{ij} S_{ij}^s \right\rangle = \left\langle u_i^r u_j^r S_{ij}^s \right\rangle$ (again using Parseval's theorem), recall that the tensor τ_{ij} is typically modeled such that total interscale energy transfer is statistically accurate, i.e. $-\left\langle \tau_{ij}^{mod} S_{ij}^r \right\rangle = -\left\langle \tau_{ij} S_{ij}^r \right\rangle$ (Meneveau & Katz 2000). For complete consistency in energetics, one might assume that an additional constraint on the enriched fields, u_i^s is required if $\left\langle \tau_{ij} S_{ij}^s \right\rangle = \left\langle \tau_{ij}^{mod} S_{ij}^s \right\rangle$. We now use Leonard's decomposition (Leonard 1975) to show that this is not the case. Consider $\mathcal{I}_2$ again,

$$\mathcal{I}_2 = \left\langle L_{ij} S_{ij}^s \right\rangle + \left\langle C_{ij} S_{ij}^s \right\rangle + \left\langle R_{ij} S_{ij}^s \right\rangle = \left\langle L_{ij} S_{ij}^s \right\rangle \tag{2.15}$$

where, $L_{ij} = \left(u_i^r u_j^r\right)^r - u_i^r u_j^r$ is the *Leonard* stress, $C_{ij} = \left(u_i^r u_j^s + u_i^s u_j^r\right)^r$ is the *cross-stress*, and $R_{ij} = \left(u_i^s u_j^s\right)^r$ is the resolved component of the small scale Reynolds stress tensor. Note that the last equality in Equation 2.15 is a consequence of Parseval's theorem. Therefore, the energy transfer due to $\mathcal{I}_2$ is only a function of Leonard stress which is a closed term in the LES equations (Eq. 2.4), and hence is not affected by the spatio-temporal inaccuracies associated with τ_{ij}^{mod}.

Figure 1 shows the interscale energetics for a periodic homogeneous isotropic turbulence simulation done on a 256^3 numerical grid at $Re \to \infty$ (with a subgrid scale model). In the present discussion, the role of the subgrid scale model has been ignored since its effect is modeled as part of the non-linear physics later. A Cartesian spectrally sharp filter is used to define large and small scales. This figure allows for the following three observations: a) While the magnitude of interscale transfer, $\mathcal{I}_1$ is substantially smaller

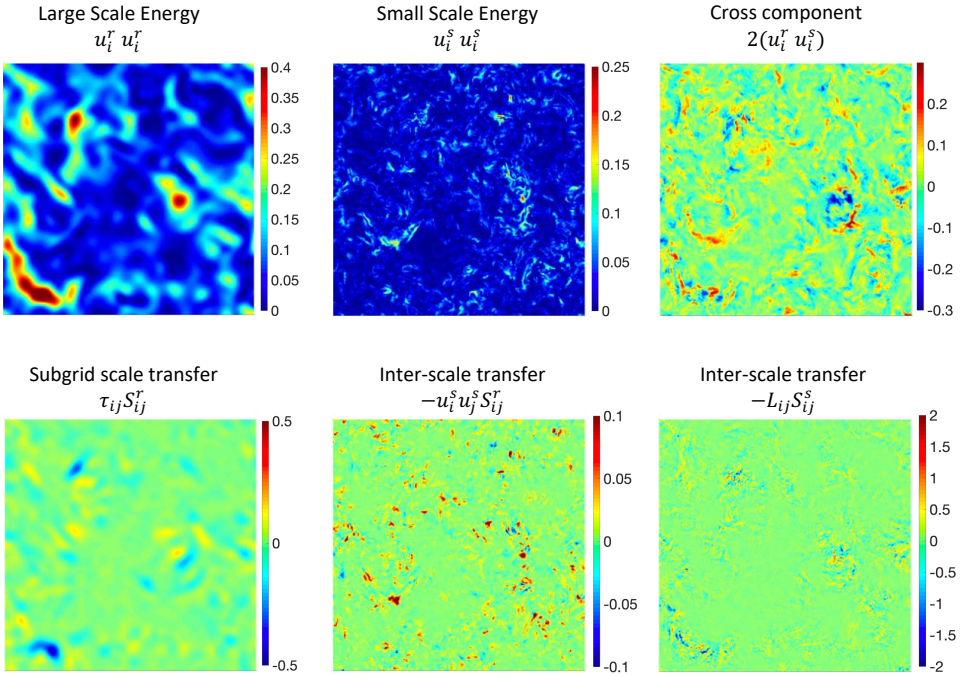

(a) Scale decomposition for 256^6 forced HIT using splitting wavenumber, $k_{co} = 16$

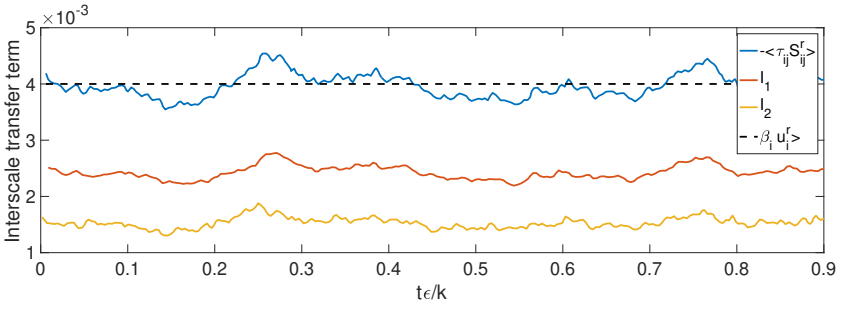

(b) Time history of the interscale transfer terms

FIGURE 1. Kinetic energy decomposition and interscale energy transfer for the Homogeneous Isotropic Turbulence (HIT) case discussed in Section 5. In subfigure (d), red and blue regions correspond to regions where there is gain and loss in large scale KE respectively. In subfigures (e) and (f) red regions depict gain in small scale KE whereas blue regions indicate loss of small scale KE.

than that of $\mathcal{I}_2$, $\mathcal{I}_1$ makes a larger contribution to the global interscale energy transfer (it is more persistently positive); b) The small scale kinetic energy does not appear spatially homogeneous over the entire domain but is rather well correlated with the interscale transfer that contributes to $\mathcal{I}_1$; and c) The terms that contribute to $\mathcal{I}_2$ appear to be correlated to the cross component of the energy, $u_i^s u_i^r$. While not shown here for brevity, these qualitative observations appear to be independent of the choice of the cutoff wavenumber selected in the inertial subrange.

While the discussion in this section regarding inter-scale energy transfer has been

presented from the perspective of single point statistical measures targeted for modeling, interested reader is referred to the substantial array of literature on inter-scale energetics in turbulent flows. Recent work by Doan *et al.* (2018) has addressed the role of non-local vortex stretching in interscale transfer of enstrophy flux for a wide range of Reynolds numbers and Johnson (2020) introduced an exact relationship between interscale energy transfer and vorticity-strain interactions. Johnson (2020) shows that scale non-local vortex stretching (large scale strain on small scale vorticity) and strain self-amplification play a more important role in interscale transfers than scale local vortex stretching. As will be shown later in Section 4, the proposed enrichment model captures the interscale tranfers via non-local vortex stretching resulting in certain vorticity alignments with large scale strain rates that are reminiscent of the behaviour of Burgers-Townsend vortices subjected to background strain.

2.2. *Temporal decorrelation of subfilter-scale turbulence*

Since, one of the requirements of the subfilter scale enrichment model is accurate temporal behavior in terms of second order statistics, i.e. $c_{ij}(\boldsymbol{x},t,\tau) = \langle u_i(\boldsymbol{x},t)u_j(\boldsymbol{x},\tau)\rangle$, it is instructive to return to Equation 2.8 and analyze its terms. However, before doing so, we will absorb the pressure non-linearity into the other terms by using the divergence free constraint. Equation 2.8 can be rewritten as

$$\partial_t u_i^s = -\underbrace{\left[u_j^r\partial_j u_i^s - \left(u_j^r\partial_j u_i^s\right)^r\right]^\perp}_{\text{Term 1 (Sweeping)}} - \underbrace{\left[u_j^s\partial_j u_i^r - \left(u_j^s\partial_j u_i^r\right)^r\right]^\perp}_{\text{Term 2 (Straining)}} - \underbrace{\left[\partial_j\left(u_i^s u_j^s - (u_i^s u_j^s)^r\right)\right]^\perp}_{\text{Term 3 (Nonlinear relaxation)}} + \underbrace{[\partial_j L_{ij}]^\perp}_{\text{Term 4 (Leonard stress source/sink)}} + \underbrace{\frac{1}{Re}\partial_j\partial_j u_i^s}_{\text{Term 5 (viscous diffusion)}} \tag{2.16}$$

where, $f_i^\perp$ is the solenoidal projection of the vector field, f_i which can be computed by solving the Poisson equation

$$f_i^\perp = f_i - \partial_i\phi^f \quad ; \quad \partial_j\partial_j\phi^f = \partial_i f_i \tag{2.17}$$

It is easy to see that Equation 2.17 can be solved exactly in spectral space (homogeneity/periodicity) as $\hat{f}_i^\perp(\boldsymbol{k}) = \left(\delta_{ij} - \frac{k_i k_j}{k_m k_m}\right)\hat{f}_j(\boldsymbol{k})$ and inviscid boundary conditions can be accommodated via specifying boundary conditions on ϕ.

For the HIT simulation shown in Figure 1, we can compute the relative magnitude of each of the terms on the RHS of Eq. 2.16 (shown in Figure 2). While this plot does not provide any information regarding the relative phase and cross-correlations among each term (sum of the mean squares of 4 terms does not give the energy of the total acceleration), it still suggests that majority of the small scale acceleration is due to the sweeping of the small scales by the large scales. The non-linear term only becomes significant at large k and only dominates the sweeping term for $k > 10k_{co}$, where k_{co} is the cutoff or the scale-separation wavenumber. Note that while the energies in Terms 2 and 4 are substantially smaller than the other terms, it does not necessarily mean that they do not affect temporal dynamics (in fact as shown in the previous section these terms cause interscale energy transfer).

In order to systematically study the decorrelating effect of each of the 4 contributors in small scale acceleration, consider the time integral of Equation 2.16,

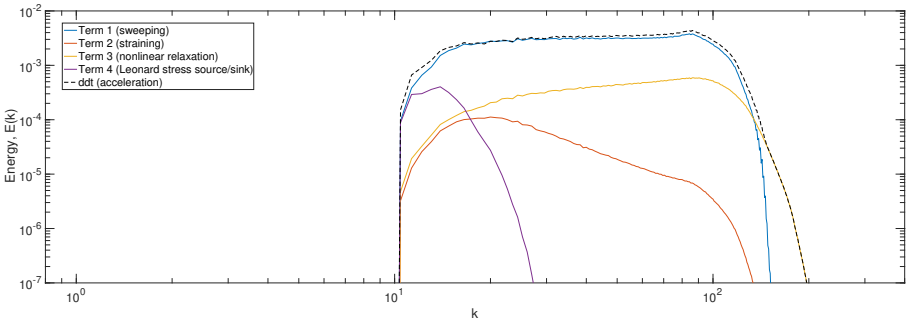

(a) Cutoff wavenumber, $k_{co} = (2/3)16$

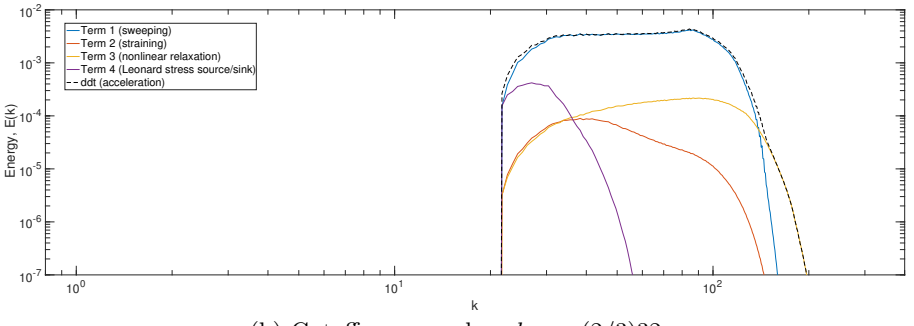

(b) Cutoff wavenumber, $k_{co} = (2/3)32$

FIGURE 2. Magnitude of each term in RHS of Equation 2.16 binned in spherical wavenumber bins. The magnitudes from each of the three equations are computed separately and then averaged for generating this figure. Note that the units of the y-axis are non-dimensionalized using the domain length and a velocity scale determined by the energy spectrum.

$$\int_t^{t+\tau} \partial_t u_i^s dt' = u_i^s(\boldsymbol{x}, t+\tau) - u_i^s(\boldsymbol{x}, t) = \int_t^{t+\tau} \mathcal{T}_1 \left\{ \boldsymbol{u}^s(\boldsymbol{x}, t'), \boldsymbol{u}^r(\boldsymbol{x}, t') \right\} dt'$$
$$+ \int_t^{t+\tau} \mathcal{T}_2 \left\{ \boldsymbol{u}^s(\boldsymbol{x}, t'), \boldsymbol{u}^r(\boldsymbol{x}, t') \right\} dt' + \int_t^{t+\tau} \mathcal{T}_3 \left\{ \boldsymbol{u}^s(\boldsymbol{x}, t') \right\} dt' + \int_t^{t+\tau} \mathcal{T}_4 \left\{ L_{ij}(\boldsymbol{x}, t') \right\} dt'$$
$$+ \int_t^{t+\tau} \mathcal{T}_5 \left\{ Re, \boldsymbol{u}^s(\boldsymbol{x}, t' \right\} dt' \quad (2.18)$$

where the terms of the form $\mathcal{T}_i$ are the 5 terms on the right hand side of Equation 2.16. Now, if we multiply both sides of the Equation above by $u_i^s(\boldsymbol{x}, t)$ and average/integrate over all $\boldsymbol{x}$ and t, we get†:

† The index notation for repeated indexing is NOT applicable in this equation.

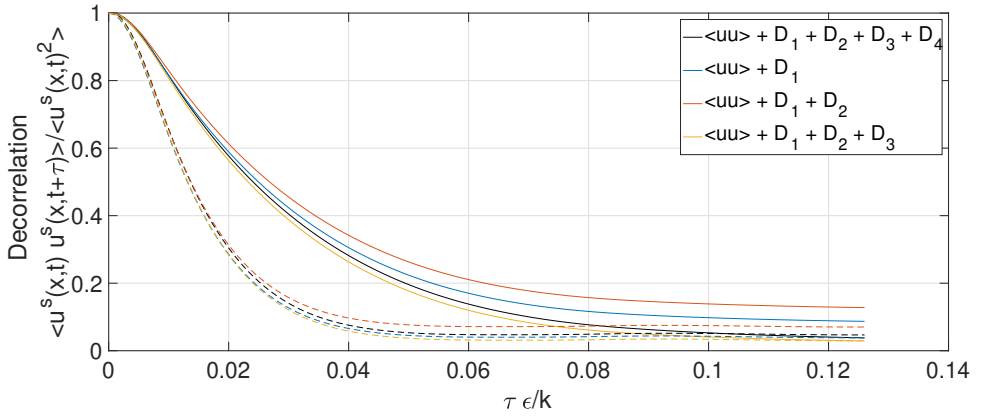

(a) Temporal decorrelation for u_1^s component

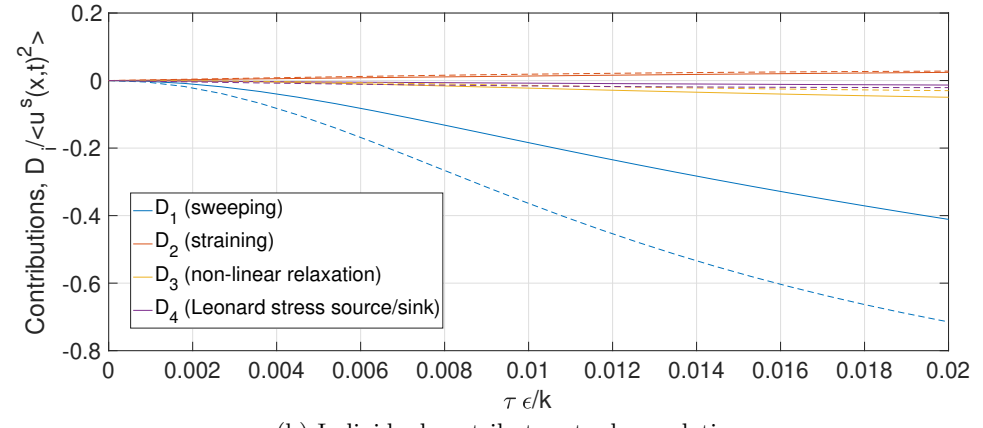

(b) Individual contributors to decorrelation

FIGURE 3. Temporal decorrelation of small scale fluctuations for the HIT case with a cutoff wavenumber; Solid lines: $k_{co} = (2/3)16$, Dashed lines: $k_{co} = (2/3)32$

$$c_i(\tau) = \langle u_i^s(\boldsymbol{x},t)u_i^s(\boldsymbol{x},t+\tau)\rangle = \langle u_i^s(\boldsymbol{x},t)u_i^s(\boldsymbol{x},t)\rangle + \underbrace{\left\langle u_i^s(\boldsymbol{x},t)\int_t^{t+\tau}\mathcal{T}_1 dt'\right\rangle}_{\mathcal{D}_1} + \underbrace{\left\langle u_i^s(\boldsymbol{x},t)\int_t^{t+\tau}\mathcal{T}_2 dt'\right\rangle}_{\mathcal{D}_2} + \underbrace{\left\langle u_i^s(\boldsymbol{x},t)\int_t^{t+\tau}\mathcal{T}_3 dt'\right\rangle}_{\mathcal{D}_3} + \underbrace{\left\langle u_i^s(\boldsymbol{x},t)\int_t^{t+\tau}\mathcal{T}_4 dt'\right\rangle}_{\mathcal{D}_4} + \underbrace{\left\langle u_i^s(\boldsymbol{x},t)\int_t^{t+\tau}\mathcal{T}_5 dt'\right\rangle}_{\mathcal{D}_5} \quad (2.19)$$

Note that in the high Reynolds number limit, $Re \to \infty$, the viscous decorrelation $\mathcal{D}_5(\tau) \to 0$ as long as the solution u_i^s does not contain a finite-time singularity! The decorrelation, $c_1(\tau)$ along with the 4 contributions from Equation 2.19 for the HIT case

are shown in Figure 3. Several observations are immediately evident from these results (pertaining to the $k_{co} = (2/3)16$ case). The sweeping term dominates the decorrelation of small scales at early and intermediate times ($0.01 < \tau\varepsilon/k < 0.055$). At early times (subfigure (c)) $\tau\varepsilon/k < 0.004$, the sweeping term overpredicts the true decorrelation and the straining term corrects it by keeping the small scales correlated. This is expected since the straining term adds energy via phase alignment (RDT) which is consistent with the interscale energy transfer observations (see $\mathcal{I}_1$) made in Figure 1. At late times ($\tau\varepsilon/k > 0.045$), the non-linear term causes non-negligible decorrelation (see subfigure a), compensating for the correlating effect of the straining term. The Leonard stress source/sink term does not appear to affect the overall statistical decorrelation of the flow field. In other words, while the term itself may be non-negligible (see Figures 2 and 1), its spatial averaged counterpart does not appear to induce substantial decorrelation at time scales that are relevant to subfilter-scale motion. This is a very convenient attribute of this source term since its effect can be modeled separately using instantaneous Leonard stresses from the resolved scales. For the case with $k_{co} = (2/3)16$ cutoff, a large part of the overall decorrelation occurs due to the linear interactions (sweeping and straining) since the larger scales are more energetic in $k_{co} = (2/3)32$ case.

These observations play a key role in development of the model for small scale enrichment as described in the next section.

3. Gabor mode representation

3.1. *Wavelet/Wavepacket representation*

The Gabor modes/wavepackets employed in our formulation, represent a windowed Fourier transform as will be defined later in this section. Its advantages over other types of wavelet transform are limited to the *synthesis* problem (as opposed to the *sensing* problem). In general, the use of canonical wavelets such as Daubechies (see Mallat (1999)) family of wavelets (used in discrete wavelet transforms) provides more aggressive compression in degrees of freedom since these wavelets have physical supports that scale with wavelength, whereas Gabor wavepackets discussed here have the same fixed support for each wavelength. Due to this spatial coarsening, wavelets can provide more spatial localization than the Gabor transform/wavepacket. For a more comprehensive discussion of Gabor modes in the context of the broader class of tools that rely on wavelets (Farge & Schneider 2001; Goldstein & Vasilyev 2004) the reader is referred to Ghate (2018). However, we note the following two advantages of using Gabor modes in the context of the enrichment problem.

(i) The Gabor transform is more amenable to theoretical manipulation, and ideas of WKB asymptotics using scale separation can easily be incorporated theoretically, which allows for easier modeling of the temporal dynamics (Section 4). In fact, substantial contributions to turbulence theory were made in late 1990s and early 2000s using the Gabor transform (see for e.g. Nazarenko *et al.* (1999); Dubrulle *et al.* (2001, 2002); Laval *et al.* (2004)).

(ii) Notion of *compression* in degrees of freedom does not necessarily imply reduction in computational cost. In incompressible flows, the non-linearity introduced by pressure is non-local in physical space, and can be a significant challenge in 3D flows where pressure-less algorithms are not widely known. In fact, a more appropriate comparison of wavelet-based treatment of the governing equations is that with other spectral discretizations of the full equations. Schneider & Vasilyev (2010) provide an excellent review of the challenges associated with wavelet discretization of incompressible Navier-

Stokes equations. The notion of quasi-homogeneous regions along with some theoretical simplifications (since the oscillatory aspect is provided by Fourier basis) associated with WKB-RDT makes the treatment of this non-local non-linearity associated with pressure, very tractable.

3.2. *Quasi-homogeneity assumption*

We will introduce the notion of quasi-homogeneity in the context of simulations of wall-bounded turbulence by introducing the following three length scales:

(i) The domain length scale (boundary layer height): δ. The flow is highly inhomogeneous at this length scale due to the viscous and kinematic effects of the wall.

(ii) A coarse LES grid scale, which is also the filter width used to separate the small scales from the resolved scales: Δ

(iii) A windowing scale, Δ_w such that $\Delta_w \gg \Delta$ and $\delta \gg \Delta_w$.

If we window the subfilter-scale (based on Δ) field using an appropriate windowing function (here taken to be a Gaussian) of characteristic length, Δ_w and centered at coordinate $\boldsymbol{x}_0$ we obtain:

$$\boldsymbol{u}_w(\boldsymbol{x}, \boldsymbol{x}_0, \Delta_w) = f(\boldsymbol{x} - \boldsymbol{x}_0, \Delta_w)\boldsymbol{u}(\boldsymbol{x}) \tag{3.1}$$

where $\boldsymbol{u}(\boldsymbol{x})$ is an instantaneous snapshot of the velocity field. We now make the following hypothesis: *For a certain choice of Δ_w, the vector field $u_w(\boldsymbol{x}, \boldsymbol{x_0}, \Delta_w)$ is locally homogeneous over length scales smaller than Δ_w*; this will be referred to as the *quasi-homogeneity* assumption. If we argue that the length scale of this *quasi-homogeneous* region $\left(\mathcal{D}_{QH}(\boldsymbol{x}_0) \subset \mathcal{R}^3\right)$ is smaller than the window support, then the following deductions regarding $\boldsymbol{u}_w(\boldsymbol{x}, \boldsymbol{x}_0, \Delta_w)$ immediately follow:

(i) An energy error-minimizing representation (Proper orthogonal decomposition, or Karhunen-Loeve expansion) of $\boldsymbol{u}_w(\boldsymbol{x}, \boldsymbol{x}_0, \Delta_w)$ which is also the most optimal representation (in terms of modes used), is in fact the Fourier representation (Lumley 1970). It is important to acknowledge that strictly speaking, this result's practical use is limited to $\boldsymbol{u}_w(\boldsymbol{x}, \boldsymbol{x}_0, \Delta_w) \subset \mathcal{C}^2(\mathcal{D}_{QH})$ due to uniform convergence of the Fourier series.

(ii) A stochastic field that is statistically equivalent (up to second order) to $\boldsymbol{u}_w(\boldsymbol{x}, \boldsymbol{x}_0, \Delta_w)$ for $(\boldsymbol{x} - \boldsymbol{x}_0) \in \mathcal{D}_{QH}$ can be written in terms of the stochastic Fourier-Stieltjes integral (see Batchelor (1953)),

$$\boldsymbol{u}_s(\boldsymbol{x}) = \int_{\boldsymbol{k} \in \mathcal{R}^3} e^{i\boldsymbol{k}\cdot\boldsymbol{x}} d\boldsymbol{Z}(\boldsymbol{k}) \tag{3.2}$$

where the stochastic vector field $\boldsymbol{Z}(\boldsymbol{k})$ has uncorrelated increments $\langle dZ_i(\boldsymbol{k}) dZ_j(\boldsymbol{k}')\rangle = \delta(\boldsymbol{k} - \boldsymbol{k}')\phi_{ij}(\boldsymbol{k})d\boldsymbol{k}$ where the spectral tensor, $\phi_{ij}(\boldsymbol{k})$ is the Fourier transform of the two-point Reynolds stress tensor, $R_{ij}(\boldsymbol{r}) = \langle u_i(\boldsymbol{x}) u_j(\boldsymbol{x} - \boldsymbol{r})\rangle$.

(iii) Equation 3.2 can be discretized efficiently by sampling wavenumbers following the ideas of Kraichnan (1970) and Fung *et al.* (1992) and as such the field, $\boldsymbol{u}_s(\boldsymbol{x})$ can be represented very efficiently in terms of $d\boldsymbol{Z}(\boldsymbol{k})$. However, any stochastic equivalent must also decay/attenuate to 0 for $\boldsymbol{x}$ outside of $\mathcal{D}_{QH}(\boldsymbol{x}_0)$. Thus, the random processes/modes must also carry appropriate support functions centered at $\boldsymbol{x}_0$. We will refer to these $d\boldsymbol{Z}(\boldsymbol{k}, \boldsymbol{x}_0, \Delta_w)$ random samplings as *Gabor modes* and rewrite the synthesis equation 3.2 as:

$$\boldsymbol{u}_s(\boldsymbol{x}, \boldsymbol{x}_0, \Delta_w) = \int_{\boldsymbol{k} \in \mathcal{R}^3} e^{i\boldsymbol{k}\cdot\boldsymbol{x}} d\boldsymbol{Z}(\boldsymbol{k}, \boldsymbol{x}_0, \Delta_w) \tag{3.3}$$

At this stage, it is essential to draw the distinction between the windowed field, $\boldsymbol{u}_w(\boldsymbol{x}, \boldsymbol{x}_0, \Delta_w)$ and the synthetic field, $\boldsymbol{u}_s(\boldsymbol{x}, \boldsymbol{x}_0, \Delta_w)$. These two fields are not the same,

and the choice of $d\boldsymbol{Z}(\boldsymbol{k}, \boldsymbol{x}_0, \Delta_w)$ is not made to approximate $\boldsymbol{u}_w$ and as such $d\boldsymbol{Z}(\boldsymbol{k}, \boldsymbol{x}_0)$ are not the POD modes of $\boldsymbol{u}$. In fact, any choice of $d\boldsymbol{Z}(\boldsymbol{k}, \boldsymbol{x}_0, \Delta_w)$ that satisfies the compactness requirement for $\boldsymbol{u}_s(\boldsymbol{k}, \boldsymbol{x}_0, \Delta_w)$ and the requirement:

$$\frac{\langle dZ_i(\boldsymbol{k}, \boldsymbol{x}_0) dZ_j(\boldsymbol{k}', \boldsymbol{x}_0)\rangle}{d\boldsymbol{k}} = \boldsymbol{\phi}_{ij}(\boldsymbol{k}, \boldsymbol{x}_0) = \int_{\boldsymbol{r}\in\mathcal{R}^3} \langle u_i(\boldsymbol{x} - \boldsymbol{x}_0, \boldsymbol{x}_0) u_j(\boldsymbol{x} - \boldsymbol{x}_0 - \boldsymbol{r}, \boldsymbol{x}_0)\rangle \, e^{-i\boldsymbol{k}\cdot\boldsymbol{r}} d\boldsymbol{r} \tag{3.4}$$

will result in $\boldsymbol{u}_s(\boldsymbol{x}, \boldsymbol{x}_0, \Delta_w)$ with the same second order spatial statistics as $\boldsymbol{u}_w(\boldsymbol{x}, \boldsymbol{x}_0)$ as $d\boldsymbol{k} \to 0$.

3.3. *Discrete Gabor modes and scale separation*

We now formalize the procedure for generation of $\boldsymbol{u}_s$ which requires us to first identify the length scale, Δ_w used to window the small scale field, $\boldsymbol{u}$. It is obvious that for $\boldsymbol{u}_w(\boldsymbol{x}, \boldsymbol{x}_0)$ to preserve the statistical characteristics of $\boldsymbol{u}(\boldsymbol{x})$ for $\boldsymbol{x} \in \mathcal{D}_{QH}(\boldsymbol{x}_0)$, we require Δ_w to be much larger than the largest relevant scale present in $\boldsymbol{u}(\boldsymbol{x})$, $\boldsymbol{x} \in \mathcal{D}_{QH}(\boldsymbol{x}_0)$. This requirement is simply $\varepsilon = \Delta/\Delta_w \ll 1$ since the scale splitting filter width is Δ. We will refer to parameter ε as the *scale-separation* parameter.

The Gabor transform of the small scale field, $\boldsymbol{u}(\boldsymbol{x})$ is defined as†:

$$\hat{\boldsymbol{u}}(\boldsymbol{x}_0, \boldsymbol{k}, \varepsilon) = \int_{\boldsymbol{x}\in\mathcal{R}^3} \boldsymbol{u}(\boldsymbol{x}) f\left(\varepsilon(\boldsymbol{x}_0 - \boldsymbol{x})\right) e^{i\boldsymbol{k}\cdot(\boldsymbol{x}_0 - \boldsymbol{x})} d\boldsymbol{x} \tag{3.5}$$

where $f(\boldsymbol{x})$ is a smooth, compact support window function, and the parameter ε controls the window width. It is easy to state the analogy between $\hat{\boldsymbol{u}}(\boldsymbol{k}, \boldsymbol{x}_0, \varepsilon)$ and the stochastic mode, $d\boldsymbol{Z}$:

$$d\boldsymbol{Z}(\boldsymbol{x}_0, \boldsymbol{k}, \varepsilon) \sim (2\pi)^3 \hat{\boldsymbol{u}}(\boldsymbol{x}_0, \boldsymbol{k}, \varepsilon) e^{-i\boldsymbol{k}\cdot\boldsymbol{x}_0} \tag{3.6}$$

The main property that is used implicitly throughout this work is the following differentiation property:

$$\widehat{\frac{\partial u_i}{\partial x_j}} = i k_j \hat{u}_i + \mathcal{O}(\varepsilon) \tag{3.7}$$

The impact of these $\mathcal{O}(\varepsilon)$ errors on the quality of the solution is detailed in Appendix A in the context of divergence error (for two different choices of ε).

The synthesis of a small scale field induced by the Gabor modes requires sampling of the stochastic modes $d\boldsymbol{Z}(\boldsymbol{x}_0, \boldsymbol{k}, \varepsilon)$. Each Gabor mode thus, carries the following 4 variables that define it:

(i) A complex valued vector amplitude: $\boldsymbol{a}$
(ii) A real-valued wave vector: $\boldsymbol{k}$
(iii) A real-valued location in the physical domain: $\boldsymbol{x}_0$
(iv) Support function, $f(\boldsymbol{x} - \boldsymbol{x}_0)$ defined in the neighborhood of $\boldsymbol{x}_0$.

Due to the uncorrelated character of the increments/modes, $d\boldsymbol{Z}$, the most appropriate choice for the support function is a trigonometric window such as a cosine window which will be used throughout this paper. This choice is largely influenced by the arguments previously made by Xiong *et al.* (2004).

† This definition is slightly different from the one seen in textbooks (Debnath & Shah 2002) where the term $e^{i\boldsymbol{k}\cdot(\boldsymbol{x}-\boldsymbol{x}_0)}$ is replaced by $e^{i\boldsymbol{k}\cdot\boldsymbol{x}}$. The difference between the two is a simple modulation/phase factor $e^{-i\boldsymbol{k}\cdot\boldsymbol{x}_0}$, and the definition stated here is primarily intended to make the definition consistent with Equation 3.1 and simplify some of the properties pertaining to its differentiation.

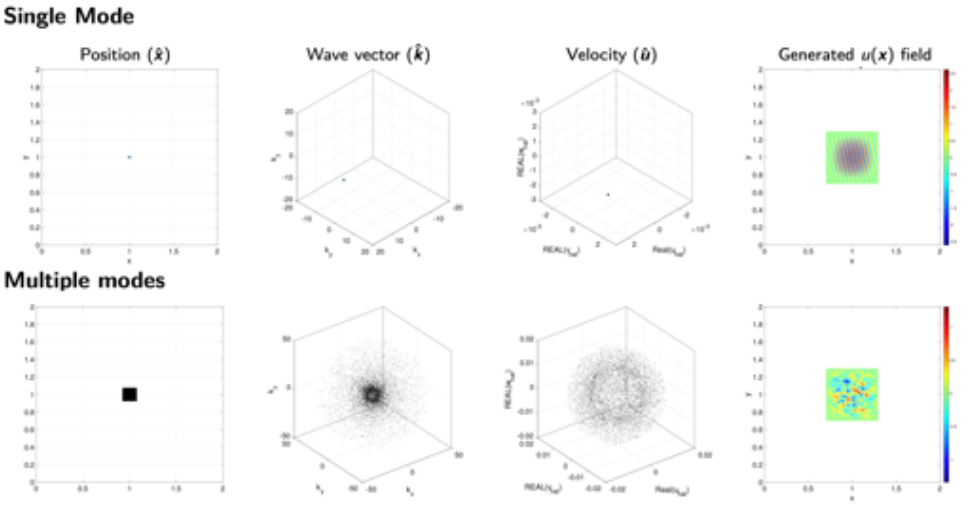

FIGURE 4. Small-scale velocity induced by Gabor modes

In order to compute the induced velocity field at a point, $\boldsymbol{x}$, we need to simply sum the contribution from each of the modes in the neighborhood of $\boldsymbol{x}$ (its quasi-homogeneous region) where the contribution from each is simply $\delta\boldsymbol{u}(\boldsymbol{x}) = \boldsymbol{a}f(\boldsymbol{x}-\boldsymbol{x}_0)e^{i\boldsymbol{k}\cdot(\boldsymbol{x}-\boldsymbol{x}_0)}$. In principle, this is a fairly expensive calculation; each quasi-homogeneous region could contain hundreds of Gabor modes, since the support function is defined by the quasi-homogeneous region it resides in, as opposed to its wavenumber. However, the calculation can be substantially accelerated by making all the modes within a quasi-homogeneous region, share a single support function. As the modes travel in space, their support envelopes change depending on the quasi-homogeneous region they lie within. This assumption is consistent with the fact that quasi-homogeneous regions are defined based on flow properties, and not the Gabor modes.

The synthesis of the velocity field for homogeneous isotropic turbulence using Gabor modes seeded in quasi-homogeneous regions is shown in Figure 4. In this illustration, the size of a quasi-homogeneous region is set to $(\Delta_{QHx}, \Delta_{QHy}, \Delta_{QHz}) = (2\Delta_x, 2\Delta_y, 2\Delta_z)$, where Δ_i is the coarse LES grid spacing in ith direction. The support length is taken to be $(\Delta_{wx}, \Delta_{wy}, \Delta_{wz}) = (2\Delta_{QHx}, 2\Delta_{QHy}, 2\Delta_{QHz})$. This choice implies a value of 0.25 for the scale separation parameter, ε and is a theoretical upper bound for the overlapping implied by the cosine support functions. The spatial location of each mode (x_j, where j is used to index a specific mode) within a quasi-homogeneous region is randomly sampled from a uniform distribution.

The velocity induced by m total modes present within a quasi-homogeneous region centered at $\boldsymbol{x}_0$ at an arbitrary point, $\boldsymbol{x}$ in the domain is given as

$$\begin{aligned}\boldsymbol{u}_s(\boldsymbol{x},\boldsymbol{x}_0) &= \sum_{j=1}^{m} f(\boldsymbol{x}-\boldsymbol{x}_j)\boldsymbol{a}_j e^{i\boldsymbol{k}_j\cdot(\boldsymbol{x}-\boldsymbol{x}_j)} \approx f(\boldsymbol{x}-\boldsymbol{x}_0)\sum_{j=1}^{m}\boldsymbol{a}_j e^{i\boldsymbol{k}_j\cdot(\boldsymbol{x}-\boldsymbol{x}_j)} \\ &= f(\boldsymbol{x}-\boldsymbol{x}_0)\sum_{j=1}^{m}\left\{\boldsymbol{a}_j e^{-i\boldsymbol{k}_j\cdot(\boldsymbol{x}_j-\boldsymbol{x}_0)}\right\} e^{i\boldsymbol{k}_j\cdot(\boldsymbol{x}-\boldsymbol{x}_0)} = f(\boldsymbol{x}-\boldsymbol{x}_0)\sum_{j=1}^{m}\tilde{\boldsymbol{a}}_j e^{i\boldsymbol{k}_j\cdot(\boldsymbol{x}-\boldsymbol{x}_0)} \end{aligned} \quad (3.8)$$

This reconstruction shows that once the modulation for each mode ($\tilde{\boldsymbol{a}}_j = \boldsymbol{a}_j e^{-i\boldsymbol{k}_j\cdot(\boldsymbol{x}_j-\boldsymbol{x}_0)}$) is calculated, calculation of the velocity field requires evaluation of the sum in the last term of Equation 3.8. Appendix B is dedicated to developing an appropriate Non-uniform

Fast Fourier Transform (NUFFT) algorithm† to calculate this sum in $\mathcal{O}(nlog(n))$ (n is the number of grid points in real space), as opposed to $\mathcal{O}(mn)$ complexity (m is the number of modes) implied by Equation 3.8. For all the problems studied in this work, the size of quasi-homogeneous regions is constant throughout the domain, including wall bounded flows, since we assume that no grid stretching is used due to wall modeling in the coarse simulations. This assumption will also need to be revisited when Gabor modes are applied to problems with abrupt changes in direction of dominant transport (such as separated flows).

Finally, note that the initialization of the Gabor modes within Quasi-homogeneous regions uses the notion of isotropically sampled modes linearly distorted by the local large scale velocity gradient tensor (RDT) through a $k-$dependent time scale (Mann 1994); further details of this procedure including determination of model constants for wall-bounded flows can be found in Ghate & Lele (2017).

3.4. *Evolution ODEs for Gabor modes*

The equations governing temporal evolution of each Gabor mode can be obtained by considering the Gabor transform of the subfilter scale equations (2.8). However, the assumption of quasi-homogeneity requires a further decomposition of the resolved scales as:

$$\boldsymbol{u}^{(r)}(\boldsymbol{x},t;\Delta) = \boldsymbol{U}(\boldsymbol{x},t;\Delta,\Delta_{QH}) + \boldsymbol{U}^{r}(\boldsymbol{x},t;\Delta,\Delta_{QH}) \tag{3.9}$$

where,

$$\boldsymbol{U}(\boldsymbol{x},t) = \int_{\boldsymbol{r}\in\mathcal{R}^3} T(\boldsymbol{r}-\boldsymbol{x})\boldsymbol{u}^{(r)}(\boldsymbol{r},t)d\boldsymbol{r} \tag{3.10}$$

with $T(\boldsymbol{r}-\boldsymbol{x})$ acting as the Δ_{QH} scale filtering operator (equal to 2Δ for all the examples discussed in this paper). With this decomposition, we can derive (see Appendix C) the equations that govern the evolution of each Gabor mode located within the quasi-homogeneous region, $\mathcal{D}_{QH}(\boldsymbol{x}_0)$ over a time scale $t \in [0,\tau]$ to a leading order in the scale separation parameter, ε

$$\frac{da_i}{dt} = \left(\frac{2k_ik_m}{k^2} - \delta_{im}\right) a_j\partial_j U_m - \nu k^2 a_i + \hat{h}_i^{\perp} \tag{3.11}$$

where a_i is the complex valued velocity information in the Gabor mode and the eikonal equation for its wavenumber given as

$$\frac{dk_i}{dt} = -k_j\partial_i U_j \tag{3.12}$$

in the frame

$$\frac{dx_i}{dt} = U_i \tag{3.13}$$

where U_i, $\partial_j U_i$ is evaluated at $\boldsymbol{x}_0$. The term $\hat{h}_i^{\perp} = (\delta_{ij} - (k_ik_j)/(k_mk_m))\hat{h}_j$ comes from the non-linear term $\partial_j(u_iu_j) + \partial_j(U_i^r u_j) + \partial_j(u_iU_j^r)$. The simplest model for the non-linear term is a spectral eddy viscosity such as the one obtained using Renormalization Group (RNG) (see Canuto & Dubovikov 1996; Laval *et al.* 2001). Under this modeling assumption, we compute $\hat{h}_i^{\perp}$ as

$$\hat{h}_i^{\perp} = -\nu_t(k)k^2 a_i \tag{3.14}$$

† The special log-spaced structure of wavenumbers $\boldsymbol{k}$ can be used to substantially accelerate Greengard & Lee (2004) Type-I NUFFT algorithm further.

where the RNG model (isotropic turbulence) for the spectral viscosity is given as:

$$\nu_t(k) = \left(\nu^2 + 0.02 \int_k^\infty q^{-2} E(q) dq\right)^{1/2} - \nu \tag{3.15}$$

The Energy Spectrum, $E(k)$ in Eq. 3.15 is estimated using the Gabor modes $(\boldsymbol{k}, \boldsymbol{a})$. This is consistent with the assumptions and findings reported in Laval *et al.* (2001) where comparisons with DNS of 3D isotropic turbulence suggest that a simple *turbulent* viscosity model is sufficient to obtain accurate decay rates. We further note that in the SGS model of Dubrulle *et al.* (2002), the authors ignore this term entirely by arguing that the subgrid-subgrid interactions are negligible. This is reasonable in their analytical model since after averaging, the transport contributed by this non-linear term is negligible. However, in our synthesis problems we have noticed that the absence of the spectral viscosity (and the implied time scale), leads to non-physical increase in energy at high wavenumbers inconsistent with Kolmogorov inertial range $(-5/3)$ scaling (pile-up resulting from absence of a KE dissipation needed for finite resolution). This is consistent with the observations made by Laval *et al.* (2001) for isotropic turbulence, where they argue that the role of the local interactions in the non-linear term is to weaken the intense vortices caused by the non-local interactions from the straining term. The turbulent viscosity model based on RNG is a natural choice for regularization desired in this formulation, since it gives the desired $k^{-4/3}$ scaling for ν_t as $k \to \infty$, and k^0 scaling as $k \to 0$. Furthermore, the implied time scale also follows the $k^{-2/3}$ in the inertial subrange, as is discussed further in the next subsection.

At this stage, it is important to relate the individual contributions to small-scale temporal decorrelations discussed in Section 2.2 with the temporal evolution model of Equation 3.11-3.13. The *sweeping-effect* in Equation 2.16 is accounted for by the description of Gabor modes in a Lagrangian frame (Eq. 3.13), and the *straining-effect* is captured by the first term on the right hand side of Equation 3.11 together with the Eikonal equation 3.12. The non-linear relaxation term in Equation 2.16 is modelled using the RNG spectral viscosity closure of Equations 3.14-3.15. The Leonard stress contribution which causes negligible temporal decorrelation, but results in interscale-energy transfer is addressed next in Section 3.5. However, it is important to emphasize at this point that these aspects of the model proposed here are helpful to justify the excellent agreement in space-time correlations of the enriched fields with reference to high resolution simulations that have previously been demonstrated for wall-bounded flows in Figures 9 and 10 of Ghate & Lele (2017).

3.5. *Cartesian Leonard fields*

The effect of the Leonard stress on evolution of subfilter-scale fields can be accounted for by using a simple superposition argument where the full subfilter scale flow-fields are obtained as:

$$\boldsymbol{u}^{(s)}(\boldsymbol{x}, t) = \boldsymbol{u}^{\text{gabor}}(\boldsymbol{x}, t) + \boldsymbol{u}^{\text{leonard}}(\boldsymbol{x}, t) \tag{3.16}$$

and *Leonard* field is simply computed as:

$$\boldsymbol{u}^{\text{leonard}}(\boldsymbol{x}, t) = \tau_\Delta \partial_j \left(L_{ij}(\boldsymbol{x}, t)\right)^\perp \tag{3.17}$$

with the Leonard stress, L_{ij} introduced in Equation 2.15: Two important observations regarding the definition 3.17 can be made.

(i) Due to the quadratic non-linearity, L_{ij} has a Nyquist wavenumber equal to twice the Nyquist wavenumber of the the large scale fields $\boldsymbol{u}^{(r)}$. This is consistent with its contribution to the subfilter-scale acceleration shown in Figure 2. More importantly, all

numerical operations on $\boldsymbol{u}^{\text{leonard}}$ (such as the projection operation implied in Equation 3.17) can be performed on numerical grid that is only twice as fine as the coarse LES grid. This is in stark contrast with the numerical grid used to render the velocity fields associated with the Gabor mode contribution $\boldsymbol{u}^{\text{gabor}}$ which requires a numerical mesh that is at least a factor of 8 finer than the coarse LES mesh.

(ii) The time scale, τ_Δ is exclusively a function of the filter-length associated with the coarse-LES fields $\boldsymbol{u}^{(r)}$. It can be modeled as:

$$\tau_\Delta = \frac{c_{\text{LEO}}}{k_\Delta \sqrt{\int_{k_\Delta}^{\infty} E(k) dk}} \tag{3.18}$$

where k_Δ is the Nyquist wavenumber of the large scales $\boldsymbol{u}^{(r)}$ and $c_{\text{LEO}} = 1.2$ is a model constant, and the spectrum $E(k)$ can be approximated using the Gabor modes. The reader is referred to recent work by Kelly (2018) who reviews the different timescales used in literature, and the choice in Equation 3.18 corresponds to $p = 0$ in generic form given in Kelly (2018). Note that the constant, c_{LEO} is a calibrated (using isotropic turbulence) model constant and does not depend on wavenumber as long as the scale separation is performed in the inertial subrange.

4. Homogeneous Isotropic turbulence

4.1. *Description of baseline simulations*

Consider a forced HIT LES at $Re \to \infty$, performed on a sequence of numerical grids starting from 32^3 through 512^3. The absence of molecular viscosity necessitates the use of a robust subgrid scale model to balance the production of turbulent kinetic energy without causing aliasing of resolvable fields. All simulations reported in this section were performed using Fourier-collocation with $2/3rd$ dealiasing (explicit filtering), and used the Sigma (Nicoud *et al.* 2011) SGS closure with a grid independent model constant of 1.3. The flow is forced in Fourier space by choosing random modes at each time step within $k = 1$ and $k = 2$ spherical shells, thereby prescribing the overall turbulent dissipation rate for the simulation (see Carati *et al.* (1995) for details). The parameters that characterize the isotropic turbulence studied in this section are provided in Table 1. The domain size is the conventional $2\pi \times 2\pi \times 2\pi$, and the simulation is allowed to reach an equilibrium state by an initial spin up time of approximately $10q/\varepsilon$ (q is the turbulent kinetic energy) prior to performing any analysis. Figure 6 shows that all simulations exhibit reasonable scale invariance in terms of spatial distribution of kinetic energy (since production is completely resolved for all cases), with some departure from the $-5/3$ slope occurring beyond a wavenumber that corresponds to approximately half of the Nyquist wavenumber.

Gabor modes are seeded within 32^3 simulation and the effective full velocity fields are visualized on a 256^3 numerical grid, which implies a factor of 8 enrichment (in each spatial dimension), and the independent LES simulation performed on 256^3 numerical grid will serve as the benchmark for comparisons. A total of 512 Gabor modes are used in each quasi-homogeneous region ($2 \times 2 \times 2$ LES cells) implying a use of 88% fewer spatial degrees of freedom than in the 256^3 case. Such a comparison requires the ability to interpolate the 32^3 LES fields on to the 256^3 grid and Figure 7 shows that while linear interpolation is overly dissipative, using cubic splines essentially eliminates this artificial energy loss. The applications discussed in this work use zero-padding in Fourier space for upsampling in periodic directions (sinc-interpolation), and cubic spline interpolation for non-periodic directions.

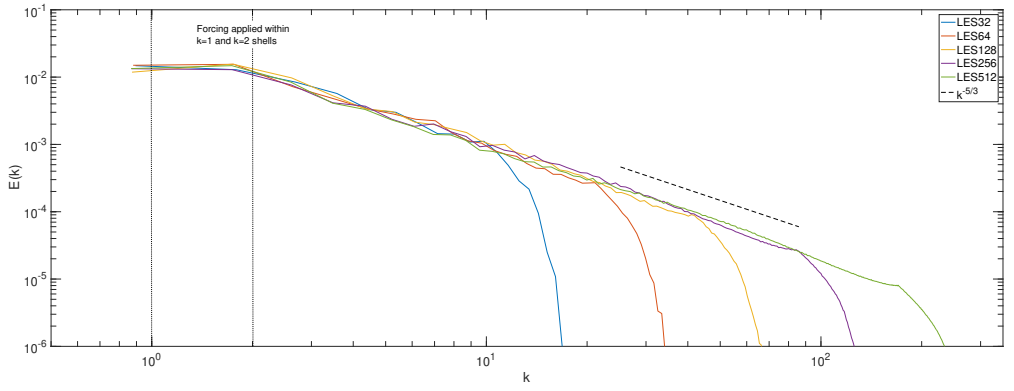

FIGURE 5. Kinetic energy spectrum for LES grids from 32^3 to 512^3

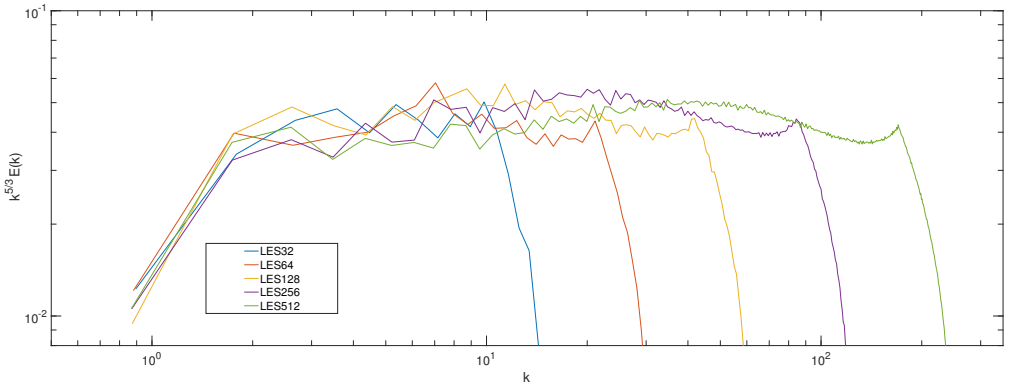

FIGURE 6. Compensated kinetic energy spectrum for LES grids from 32^3 to 512^3

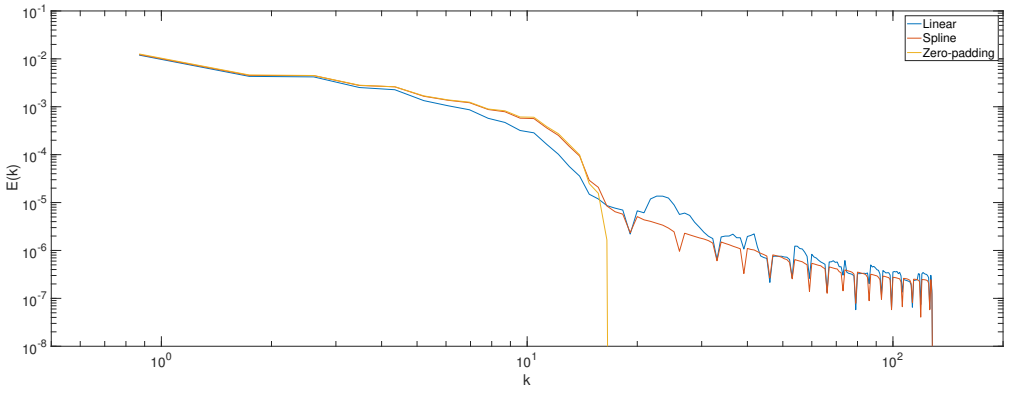

FIGURE 7. Filtering effect of interpolation of 32^3 field to the 256^3 grid. Energy losses are approximately 14% (linear), 2.5% (spline) and 0% for zero-padding.

Integral length scale, $L_0 = \frac{\pi}{k[1]}$	Velocity scale, $u_0 = \sqrt{u_j u_j}$	Turn over time scale, L_0/u_0	Kinetic energy, $u_i u_i/2$	Dissipation rate, ε
π	0.35	8.97	0.06	0.0045

TABLE 1. Characteristic parameters for the forced HIT simulations

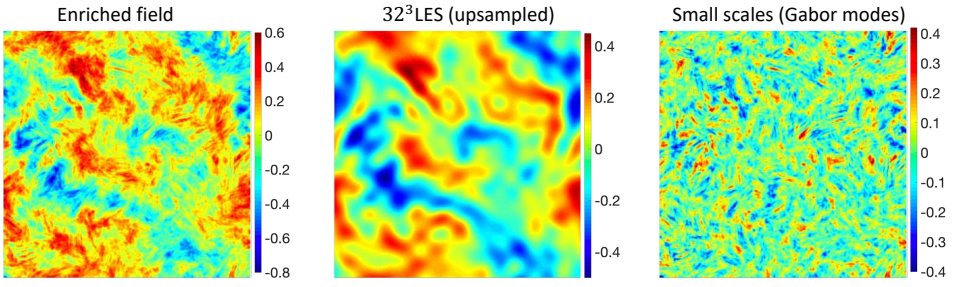

FIGURE 8. Instantaneous snapshot of v velocity field on an arbitrary $x - y$ plane. Results can be compared with Figure 1.3(a)-(c).

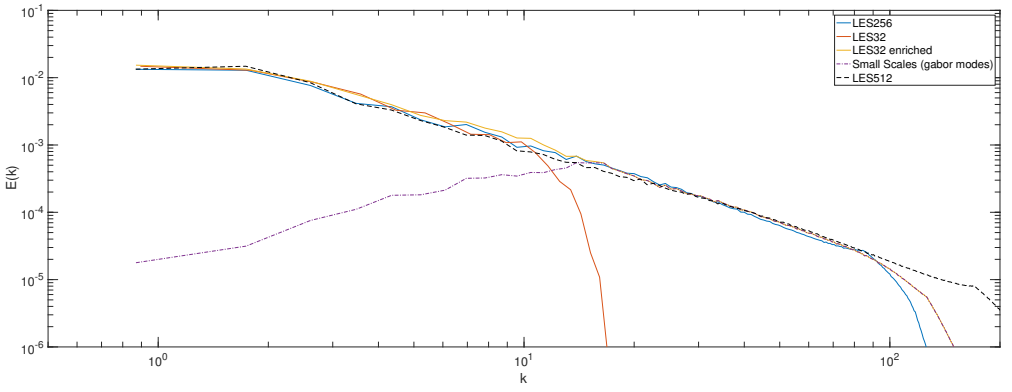

FIGURE 9. Kinetic energy spectrum for the forced HIT simulations with Gabor mode enrichment. Results can be compared with Figure 1.3(d).

4.2. *Gabor mode enriched solutions*

Figure 8 shows an instantaneous snapshot of the flow fields generated via Gabor mode enrichment of the 32^3 LES. The resulting kinetic energy spectrum (Figure 9) shows the spectral extrapolation provided by the small scales induced by Gabor modes. The 512^3 LES results are also included for reference to explain that the slight overprediction of KE in the enriched fields at high wavenumbers is not unphysical; the 256^3 LES suffers from some artificial decay in energy at very high wavenumbers due to inaccuracies in SGS modeling. The remaining observations can be summarized as follows:

Figure 10 shows that small scale kinetic energy induced by Gabor modes has localized peaks that occur due to intense straining by the large scales. This is consistent with the

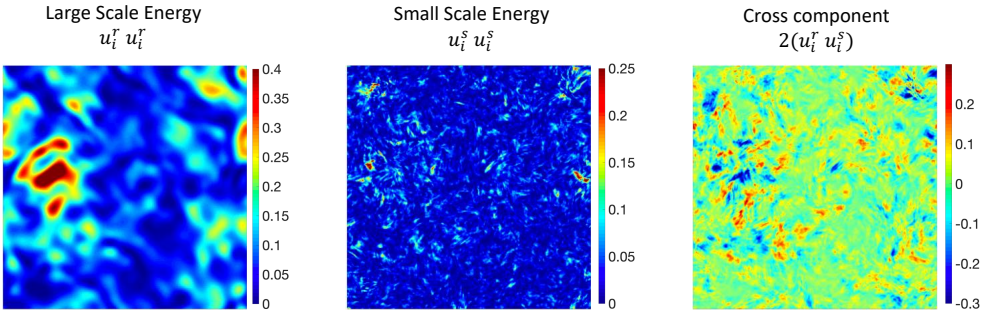

FIGURE 10. Instantaneous Kinetic energy resolved by the 32^3 LES and the small scale energy induced by Gabor modes.

observations made in section 1. The instantaneous interscale energy transfers, $\mathcal{I}_1$ and $\mathcal{I}_2$ (Equation 2.14), are shown in Figure 11 to demonstrate the tight coupling observed between the 32^3 LES and the enriched Gabor modes. The mean values for $\mathcal{I}_1$ and $\mathcal{I}_2$ are 0.0025 and 0.0018 respectively, in excellent agreement with the expected true values. Again, it is interesting to observe the strong correlation seen between small scale kinetic energy and $\mathcal{I}_1$, and cross-component of the energy and $\mathcal{I}_2$. The interscale energy transfer, $\mathcal{I}_2$ is primarily a consequence of the Gabor modes generated by the Leonard stress term in their evolution equations. The effect of these modes is localized near the filter wavenumber ($k_{co} = (2/3)16$). Spectral enrichment methods such as kinematic simulations of Flohr & Vassilicos (2000) create excellent spectral extrapolations (similar to present results), but do not capture any interscale energy transfers since Fourier modes lack spatial localization seen in Gabor modes. Figures 11c-d compare the two interscale transfer rates with the true results based on filtering of the 256^3 reference LES. The results show very promising agreement, with any quantitative differences limited to slight over-prediction of intermittency (kurtosis) in the Gabor mode enriched case. Note that such quantitative differences in higher order statistics, are not unexpected since the reference case is not grid converged (and is not a DNS), and the SGS model does contaminate the smallest scales resolved in the 256^3 LES. One dimensional spectra for u and v components are shown in Figure 12. The overall agreement with the 256^3 LES is reasonable. The discrepancies seen near $k_{co} \approx (2/3)16$ can be attributed to the cartesian (tensor-product) nature of the 32^3 LES and the spherical nature of $\boldsymbol{k}-$vectors in the enriching Gabor modes. Figure 13 shows 2d spectra for u and w components. The box drawn using red dashes is the spectral reach of the 32^3 LES (corresponding to $k_{co} = (2/3)16$). The black contour levels are made using 256^3 LES data and the colored levels are generated using enriched LES data. Figures (c) and (d) exhibit a 90^0 rotational invariance, whereas Figures (a) and (b) notably lack this invariance, consistent with the symmetries expected in isotropic turbulence (u component has a larger integral length scale in x direction, compared to y and z directions); small scales induced by Gabor modes preserve these global symmetries. Note that the 256^3 LES uses 2/3rd dealiasing, which is not needed in the enriched LES. These results reinforce the excellent comparison seen in the energy spectrum. The ability of the 32^3 LES in predicting accurate two-point correlations at large scales is noted. The enstrophy spectrum is compared in Figure 14. The large noise level in 32^3 LES is a consequence of reduced sampling size, but the effective enstrophy of the enriched LES compares quite well with the enstrophy resolved by the 256^3 LES. However, this global picture of vorticity can be quite misleading since it doesn't provide any insight regarding

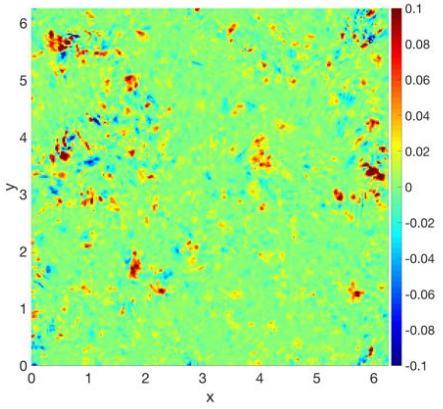

(a) Instantaneous transfer ($\mathcal{I}_1$), $-u_i^s u_j^s S_{ij}^r$

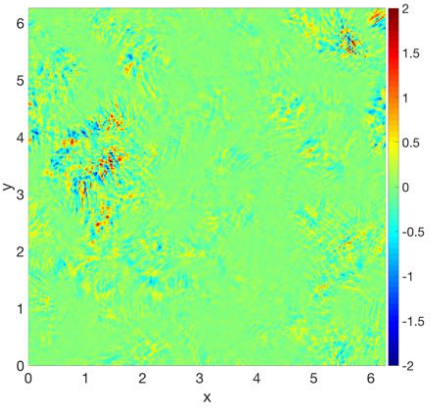

(b) Instantaneous transfer ($\mathcal{I}_2$), $-L_{ij} S_{ij}^s$

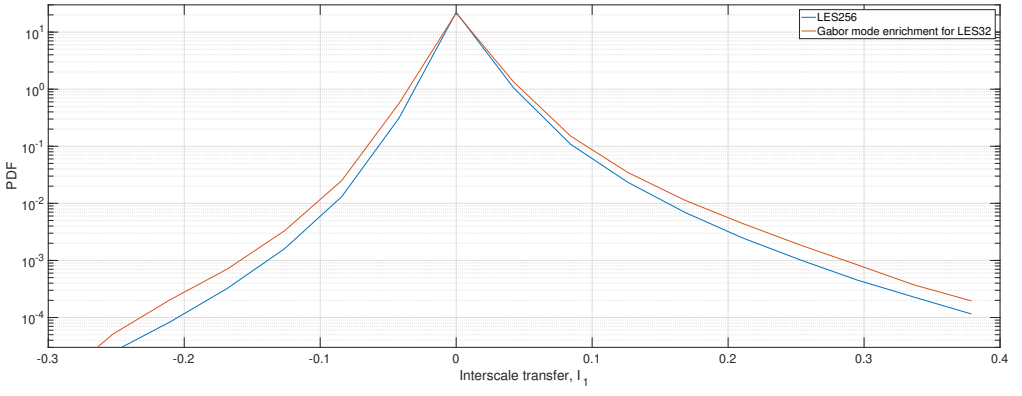

(c) PDF of $\mathcal{I}_1 = -u_i^s u_j^s S_{ij}^r$

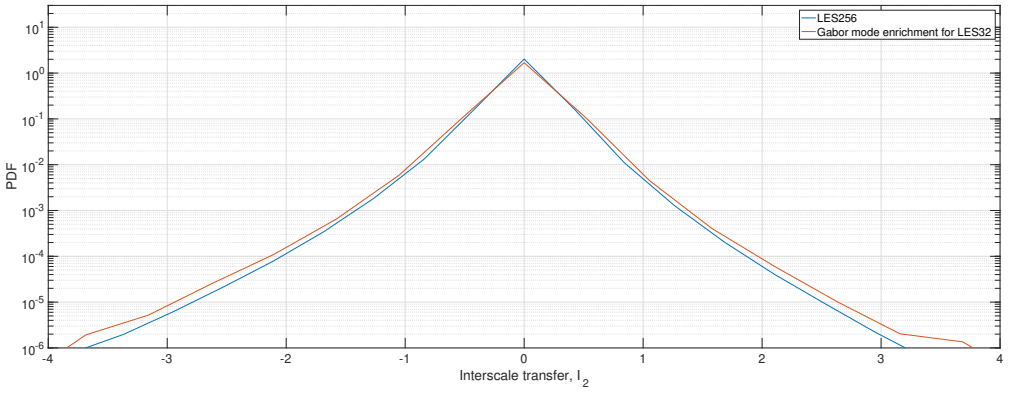

(d) PDF of $\mathcal{I}_2 = -L_{ij} S_{ij}^s$

FIGURE 11. Instantaneous energy injected into the small scales induced by Gabor modes.

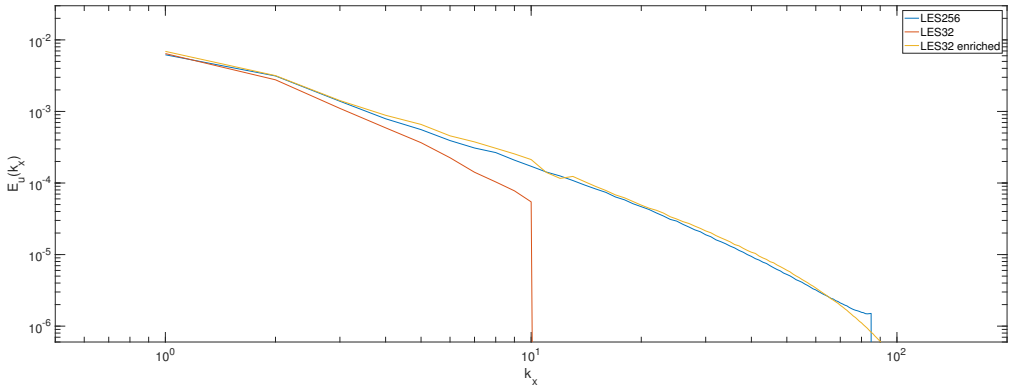

(a) u component

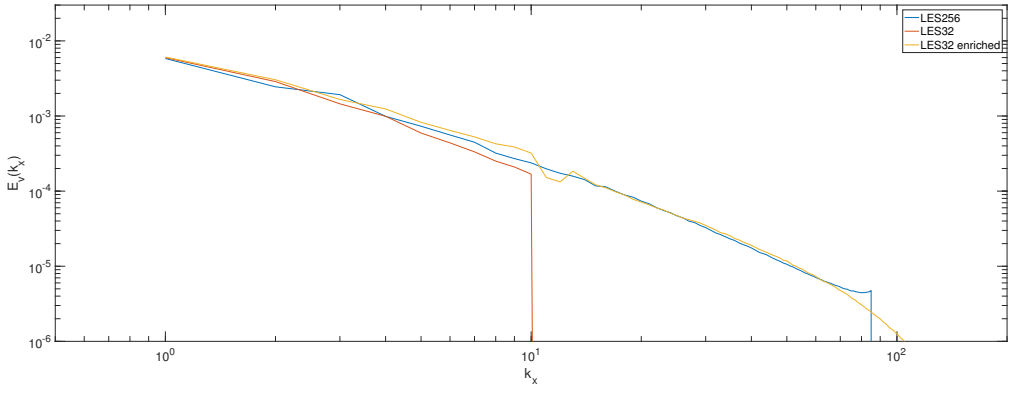

(b) v component

FIGURE 12. One dimensional, k_x spectra

spatial coherence of the vorticity field. Figures 15 and 16 show the iso-contours of vorticity magnitude in the simulated domain at contour levels of $150\varepsilon/q$ and $210\varepsilon/q$ respectively. These values are approximately 2.1 and 3 times the RMS vorticity magnitude for the 256^3 LES. It is clear that a simulation at 32^3 size does not resolve any strong vorticity of this magnitude. However, these vorticity iso-surfaces help identify two notable deficiencies in the Gabor mode induced velocity fields:

(i) The RDT-linearization in Gabor mode evolution equations leads to numerous thin vortex filaments, however the effect of non-linear terms which cause mutual distortion and entanglement (She *et al.* 1990), is noticeably absent. Laval *et al.* (2001) claim that vortex reconnection is essentially a non-linear process in which local (in scale space) interactions play an important role. Instead, the spectral viscosity used here simply prevents uninhibited stretching implied by the RDT-like terms.

(ii) The effect of quasi-homogeneous regions is very evident in the Gabor mode induced vorticity. While the thin filaments in the LES have a radii of the order of grid resolution (Kolmogorov scale in DNS), their long lengths imply a large spatial coherence. We consider the preferential orientation of the subfilter scale vorticity, $\boldsymbol{\omega}_S$ with the largest eigenvalue of the large scale (32^3 LES) strain rate tensor, $\boldsymbol{S}_R$ as shown in Figure 17. It is clear that the fine scale vorticity in the enriched case lacks some of the true physics which

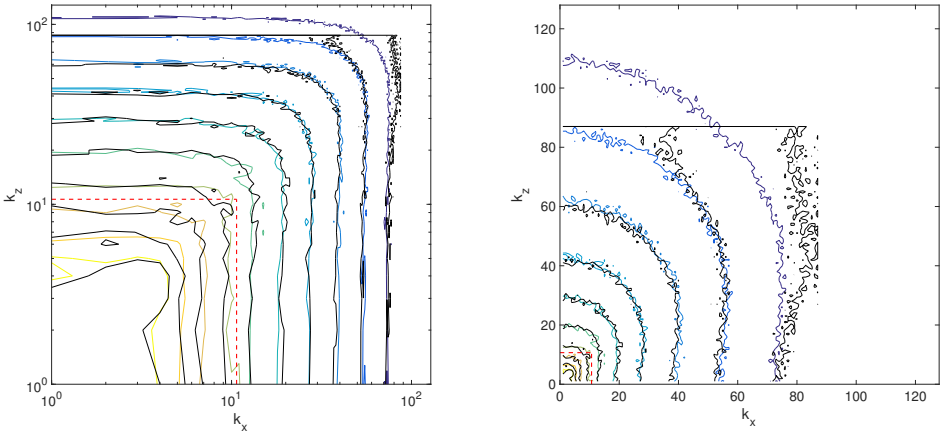

(a) $k_x - k_y$ spectrum for u (log spacing) (b) $k_x - k_y$ spectrum for u (linear spacing)

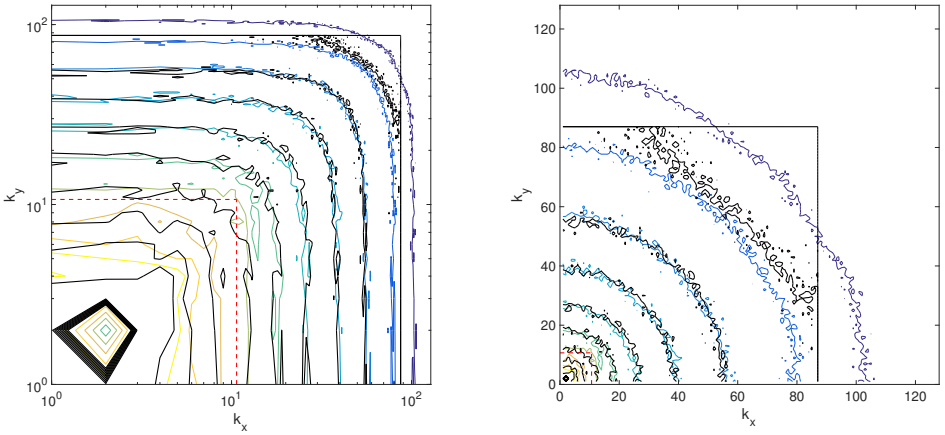

(c) $k_x - k_y$ spectrum for w (log spacing) (d) $k_x - k_y$ spectrum for w (linear spacing)

FIGURE 13. 2d spectra for u and w components. The contour levels are logarithmically equispaced between 10^{-8} and $10^{-3.5}$. Black lines: 256^3 LES, Colored lines: 32^3 LES enriched with Gabor modes

appears to be more nuanced and complex (see Figure 16a). The enriched vorticity appears to primarily consist of elongated cylindrical strucutres, reminiscent of Burgers-Townsend vortices (Townsend 1951). We observe that this subfilter-scale vorticity contained in Gabor modes is consistent with the RDT-type arguments made in vortex-based closures (Pullin & Saffman 1994; Misra & Pullin 1997; Kosović 1997) for the full subgrid scale stress tensor. Such closure models attempt to model the probability density of the subfilter vortex orientation; this statistical information is naturally present in Gabor modes due to the statistical equivalence requirement given in Equation 3.4.

Finally, it is interesting to observe that the small-scale strain rate as measured in terms of the Lund-Rogers parameter (Lund & Rogers 1994) shown in Figure 18, suggests that the field has Gaussian statistics. This appears to be consistent with the observation by Pullin & Saffman (1998) who note that volume-filling ensembles of Townsend-Burgers' vortices give poor results for the higher order moments of the longitudinal velocity

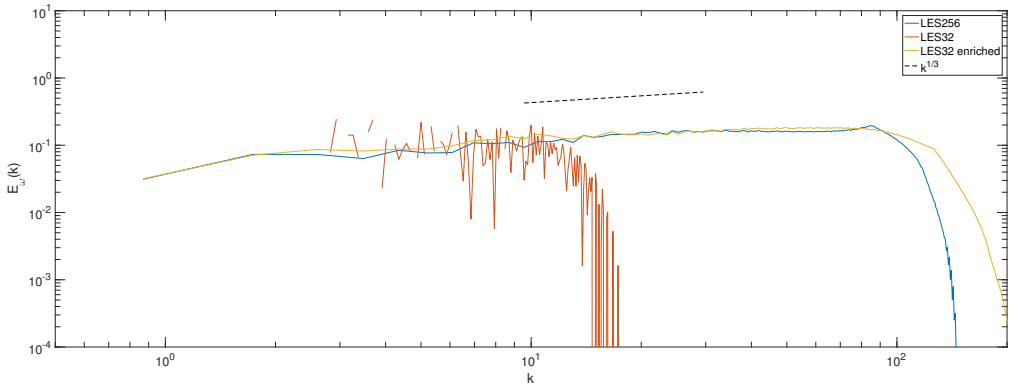

FIGURE 14. Enstrophy spectrum for the forced HIT simulations

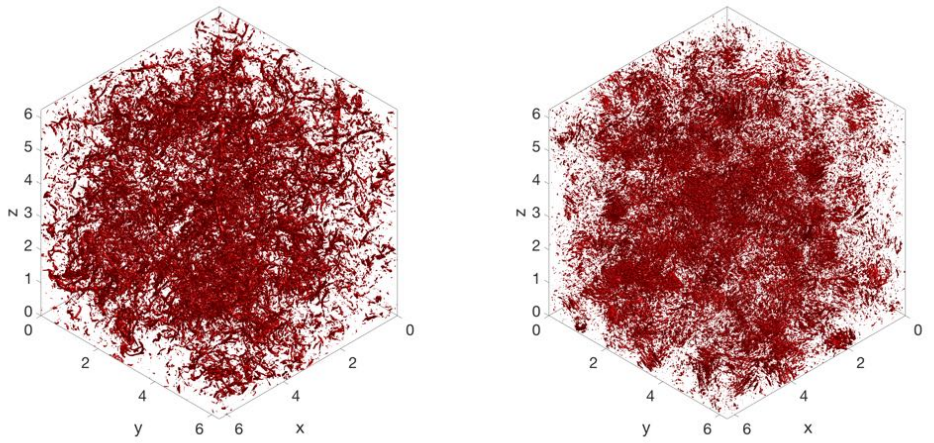

(a) 256^3 LES (b) 32^3 LES enriched with Gabor modes

FIGURE 15. Isocontours of instantaneous absolute vorticity. Contour level is $150\varepsilon/q$. The 32^3 LES does not capture any features at this vorticity level.

derivatives for isotropic turbulence. In regards to the LES results shown in Figure 17, note that while the 256^3 LES which captures the entire non-linearity at small scales also shows some preferential alignment, its PDF does not present a strong peak at the perfectly aligned state as would be expected from a highly resolved direct numerical simulation for a finite Reynolds number case. We note that the widely accepted result regarding the alignment of vorticity with the eigenvector of strain rate with the second largest eigenvalue (Ashurst *et al.* 1987; Cantwell 1992) should not be confused with the observation reported in Figure 17 which only considers the *non-local* (large scale) straining of vorticity (Hamlington *et al.* 2008). Other spectral enrichment methods relying on global Fourier modes (Flohr & Vassilicos 2000) fail to capture any of these interactions and the small scales are generated due to an entirely incoherent vorticity distribution.

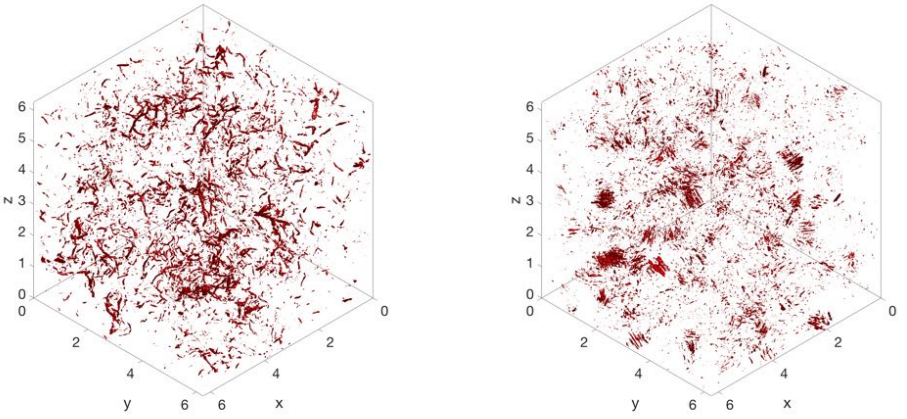

(a) 256^3 LES (b) 32^3 LES enriched with Gabor modes

FIGURE 16. Isocontours of instantaneous absolute vorticity. Contour level is $210\varepsilon/q$. The 32^3 LES does not capture any features at this vorticity level.

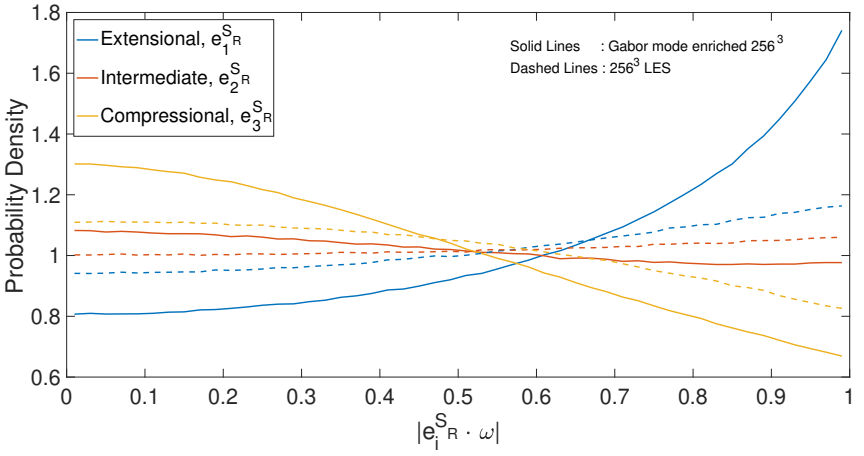

FIGURE 17. Preferential alignment of the small scale vorticity with the largest eigenvalue of the large scale strain rate tensor.

5. Half channel at $\mathrm{Re} \to \infty$

5.1. *Problem description and quality of coarse grid LES*

The second problem studied is a canonical wall bounded flow simulated as a *rough wall turbulent half-channel* (of height H), with slip boundary conditions at the top ($z = H$) and implied no-slip (stress condition for WMLES) boundary conditions at the bottom ($z = 0$). Roughness length scale z_0 is taken to be $10^{-4}H$. The domain size simulated for all cases is $(6\pi \times 3\pi \times 1)H$; such a large horizontal domain is needed due to the presence of very large streamwise-elongated coherent structures (also referred to as *very large scale motions* or VLSMs) of size $\mathcal{O}(10)$ boundary layer thickness that occur at high Reynolds numbers (del Álamo & Jiménez 2003; Tomkins & Adrian 2003; Hutchins & Marusic 2007; Balakumar & Adrian 2007). Furthermore, regardless of the total number of grid points

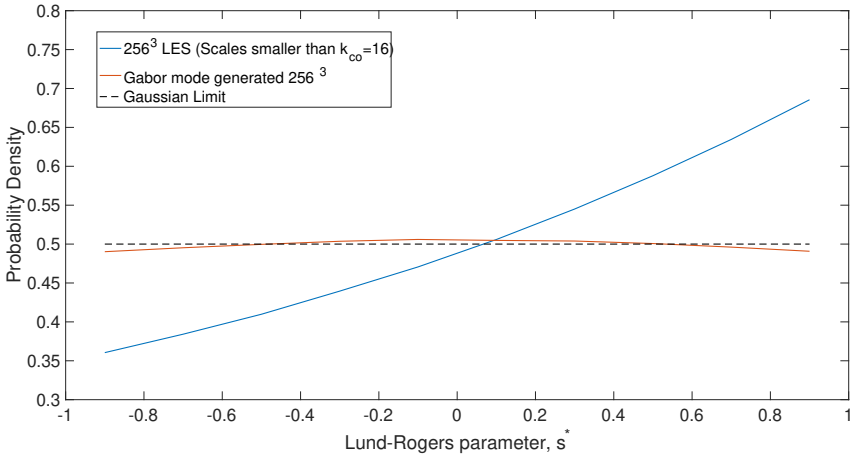

FIGURE 18. Probability distribution of small scale strain state as measured according to the parameter, $s^\star = \frac{-3\sqrt{6}\alpha\beta\gamma}{\left(\alpha^2+\beta^2+\gamma^2\right)^{3/2}}$ (Lund & Rogers 1994) where α, β and γ are the eigenvalues of the strain rate tensor (small scale). While the LES solution shows preference towards the axisymmetric extension, the Gabor mode induced small scale strain rate is largely Gaussian.

used, the cell aspect ratios for all the reported WMLES is fixed at $2\pi \times \pi \times 1$, implying a smaller grid spacing in the spanwise direction (y) than the streamwise direction (x). Note that these choices of domain length and cell aspect ratio are consistent with the findings of Lozano-Durán & Jiménez (2014) and Stevens *et al.* (2014). The simulations compared in this section correspond to the following cases:

(i) Coarse scale (low resolution) LES: Computed using $192 \times 192 \times 64$ grid points and three SGS models: Anisotropic minimum dissipation (AMD) model of Rozema *et al.* (2015) using a model constant of $1/\pi^2$ in $x-$ and $y-$ directions†, and $\sqrt{0.30}$ for z direction. These choices for the constants are consistent with those reported in Rozema *et al.* (2015) and Bae (2018); while we use a 6th order compact finite difference scheme in z, the formal order of accuracy is still second order in wall bounded flows due to the cosine-transform based Poisson solver. Although this region of second order accuracy is highly localized within the first few near wall cells, the use of Poincare constant corresponding to second order numerical accuracy is a conservative choice. Our numerical experiments suggest very low sensitivity to this choice of the constant in z direction. The results obtained for this simulation case are labelled to as `AMD64`.

(ii) Coarse scale (low resolution) LES computed using a $384 \times 384 \times 128$ grid and the AMD subgrid scale model. This second low resolution simulation is used to address some of the deficiencies seen in Gabor mode enrichment of the $192 \times 192 \times 64$ simulations. The results obtained for this simulation case are labelled to as `AMD128`.

(iii) Fine scale (high resolution) LES: Computed using $1536 \times 1536 \times 512$ grid points with the anisotropic minimum dissipation SGS model. This case will serve as a benchmark for comparison with Gabor mode enriched LES and will be denoted as `AMD512`.

(iv) Enriched LES: Each quasi-homogenenous region ($2 \times 2 \times 2$ grid cells) of the coarse LES is enriched with 512 Gabor modes. Induced flow fields are evaluated on a $1536 \times 1536 \times 512$ grid.

In addition to the simulations listed above we further include results obtained by

† Note that due to 2/3rd dealising, the filter width is taken as $\Delta_{filt} = (3/2)\Delta_{grid}$

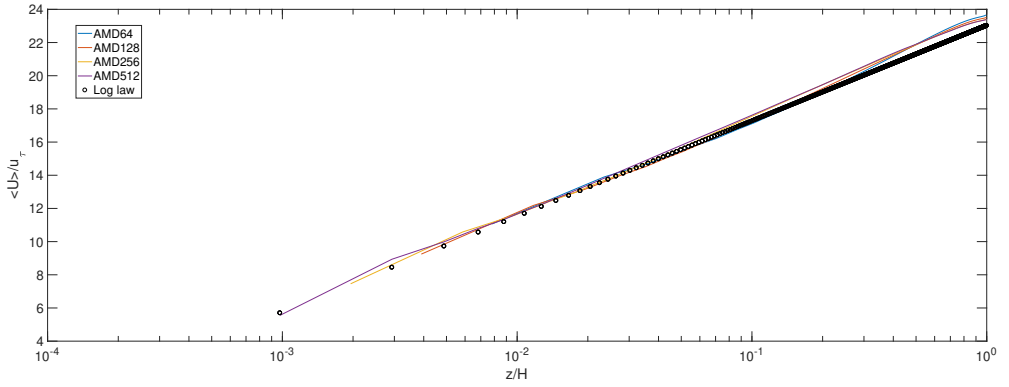

FIGURE 19. Mean profile using AMD model for grid sizes increasing from $192 \times 192 \times 64$ through $1536 \times 1536 \times 512$.

enriching the filtered `AMD512` fields; this case will be labelled as `IDEAL64`. These fields are obtained by explicitly filtering the high resolution LES data to the coarse resolution LES grids using sharp spectral filters in x and y, and the Pade-Least squares filter (Spyropoulos & Blaisdell 1996) in the wall-normal, z direction.

Since we are considering the infinite Reynolds number limit, the large eddy simulations discussed here replace the no-slip boundary condition at $z = 0$ by a shear stress boundary condition where the shear stress is computed using a simple equilibrium wall model of the form (Yang *et al.* 2017):

$$\tau_{xz} = \left[\frac{\kappa u_{\parallel}}{\ln(z_{\text{match}}/z_0)}\right]^2 \frac{u_{\text{match}}}{u_{\parallel}} \quad ; \quad \tau_{yz} = \left[\frac{\kappa u_{\parallel}}{\ln(z_{\text{match}}/z_0)}\right]^2 \frac{v_{\text{match}}}{u_{\parallel}} \tag{5.1}$$

where, κ is the von Karman constant, u_{match} and v_{match} are the instantaneous x and y velocity components at a fixed wall-normal location z_{match}, and $u_{\parallel} = \left\langle \sqrt{u^2_{\text{match}} + v^2_{\text{match}}} \right\rangle$. As highlighted by Kawai & Larsson (2012), the choice of z_{match} largely influences the so-called *log-layer mismatch* (LLM). While certain adjustments in the near wall region are commonly used by the atmospheric science community for Ekman layers (Brasseur & Wei 2010; Sullivan & Patton 2011), Bou-Zeid *et al.* (2005) and Yang *et al.* (2017)have proposed to use either spatial or temporal filtering of velocity fields (u_{match} and v_{match}), and shown that when $z_{\text{match}} = \Delta_z/2$ (first off the wall grid point), the filtering operation largely eliminated the log-layer mismatch in this infinite Reynolds number half channel problem. Results from our numerical experiments regarding the choice of z_{match} are reported in Ghate (2018). All subsequent results presented in this section use first off-the-wall grid point without any spatial and temporal filtering to compute the wall shear stress.

Figures 19 and 20 show mean velocity and Reynolds stresses for the coarse LES simulations at varying resolutions. While the mean velocity profiles clearly demonstrate lack of any log-layer mismatch at all resolutions, the streamwise velocity variances near the walls for coarse grids are larger than the values obtained using the high resolution simulations, which is contradictory to the notion of filtering. Some physical insight into these persistent over-predictions was recently proposed by Bae *et al.* (2018) who argue that the no-penetration boundary condition implicit in the equilibrium wall model used in our simulations, results in non-physical splatting of the resolved large scales. They report up to 90% over prediction of the streamwise variance in their $Re_\tau = 2000$

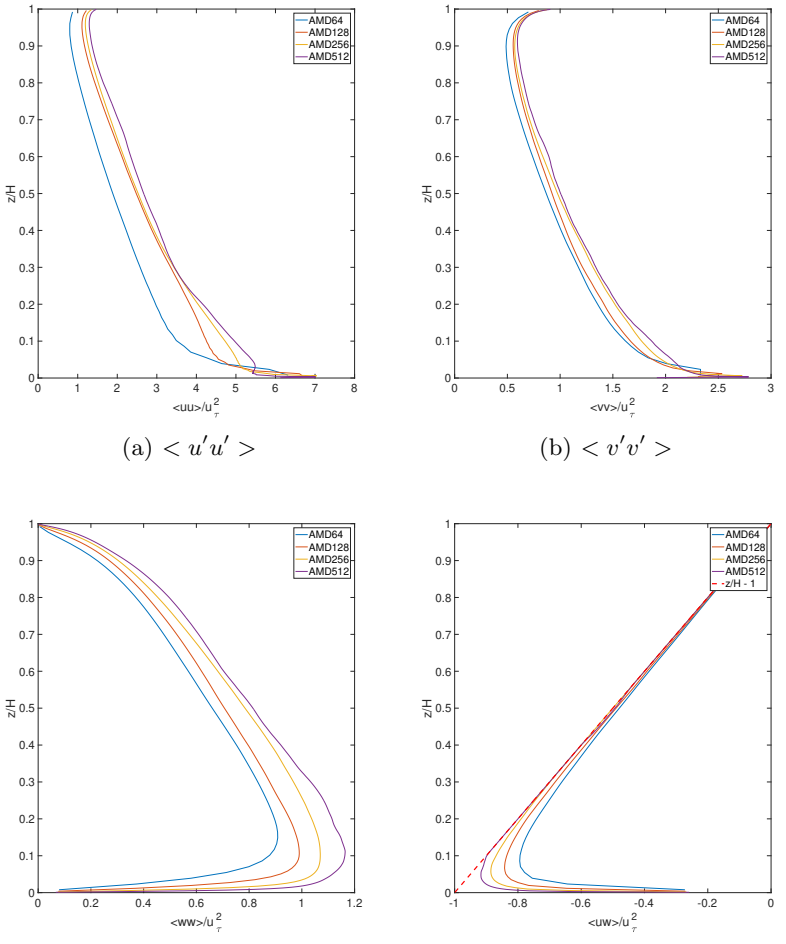

(a) $< u'u' >$ (b) $< v'v' >$

(c) $< w'w' >$ (d) $< u'w' >$

FIGURE 20. Single point second order correlations using the AMD model from grid sizes increasing from $192 \times 192 \times 64$ through $1536 \times 1536 \times 512$.

simulations using a no-slip boundary condition. While the spanwise and vertical velocity variances are smaller in the coarse LES than the high resolution LES, we will show later (using `IDEAL64`) that these variances are still larger than the expected values at the $192 \times 192 \times 64$ resolution. While these errors are not unexpected (the present results are entirely consistent with the profiles shown in Porté-Agel *et al.* (2000) for similar resolutions), it is clear that the AMD model (also true for the Sigma SGS model) over-estimates all four pertinent single point correlations at the coarsest resolution, especially in the near wall region ($z < 0.1H$). A second striking feature seen in the variance profiles is the significant under-prediction of the streamwise variance $z > 0.25H$ by the 64-point simulation. This is related to the underprediction of energy in the large streamwise coherent structure corresponding to $k_x L_x/(2\pi) \approx 2$ and $k_y L_y/(2\pi) \approx 4$ wavenumber and our numerical experiments using the Sigma SGS model and the wall-damped Smagorinsky model showed the same flaw. The grid refinement study suggests that as the LES Nyquist wavenumbers increase, this spanwise coherent structure

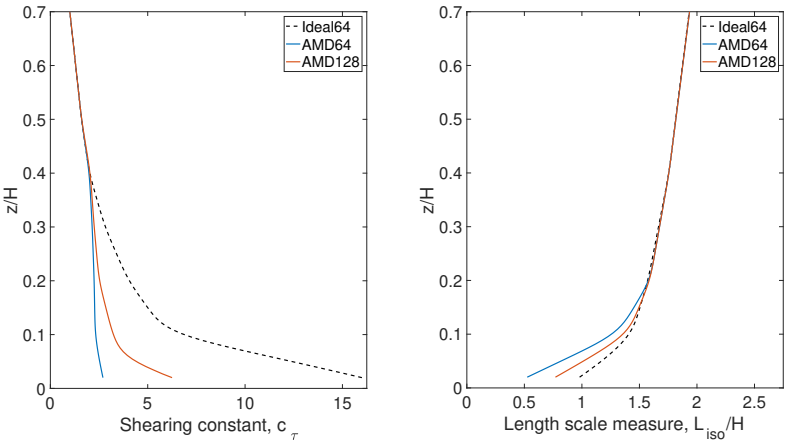

FIGURE 21. Model inputs for enrichment of the three coarse LES flow fields

becomes more energetic, especially as the coarsest mesh at $192 \times 192 \times 64$ is refined to $384 \times 384 \times 128$. This improvement can be seen in terms of single point correlations in Figure 20. This energetic large scale structure necessitates the use of such a large domain size for periodic simulations. The inability of coarse simulations to capture the correct energy in these large spanwise structures also implies that the coarse simulations inaccurately predict the integral length scales. While the total cross stress $\langle u'w' + \tau_{13}^{SGS} \rangle$ is grid independent (since a constant pressure gradient is used to drive the flow), the grid invariance of mean profiles using the AMD model, also implies that the total TKE production rate $\langle u'w' + \tau_{13}^{SGS} \rangle \frac{d<U>}{dz}$ is correctly predicted in the coarse simulations.

5.2. *Gabor mode enrichment of low resolution LES*

The three model inputs that need to be specified to initiate the Gabor modes (see Ghate & Lele (2017) for details) are the following:

(i) Minimum wavenumber, k_{min} associated with the embedded Gabor modes. This parameter is a purely geometric parameter and depends on the size of quasi-homogeneous regions defined. Since in the WMLES described above, no grid stretching is used in the vertical direction, this parameter is simply computed using the coarse LES cell width (filter width), and does not vary in the wall normal direction. The maximum sampling wavenumber is simply set to ensure that the induced fields when resolved on a $1536 \times 1536 \times 512$ grid, do not alias.

(ii) Pre-distortion isotropic length scale measure, L_{iso}. Based on the discussion regarding inadequacy of coarse LES in predicting energy in the streamwise streaks, we use the following choice: $L_{iso}(z) = c_L \sqrt{L_x^v(z) L_y^v(z)}$ where the constant $c_L = 1/0.67$ to ensure that in the limit of isotropy, L_{iso} is the integral length scale of isotropic turbulence. Note the preference of using spanwise velocity lengthscales over streamwise velocity length scale in order to reduce the influence of streamwise variance underprediction error in coarse LES, on the enriched fields. For stably stratified Ekman layer (as in Ghate & Lele (2017)) the choice of streamwise velocity length scales was satisfactory because the stable stratification prevented the integral length scales from growing larger than boundary layer height. Our experience suggests that for a larger value of L_{iso} (if u length scales are used), implying larger $(k_{min} L_{iso})$, a larger shearing constant c_τ is needed in

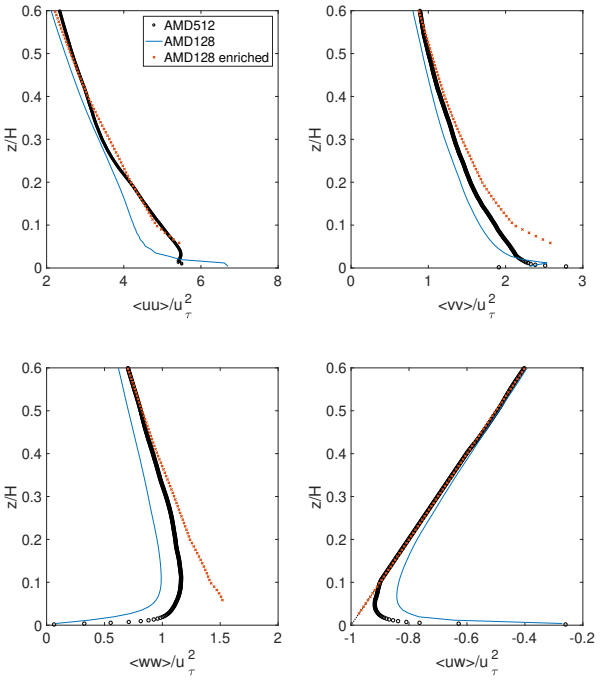

FIGURE 22. Single point correlations as a function of height for the AMD128 case enriched using Gabor modes.

order to obtain the correct Reynolds stresses, thereby creating subfilter scales that are overly anisotropic.

(iii) The shearing constant c_τ which is computed by minimizing the least squares error in the Reynolds stress, $< u'w' >$ (see Appendix B in Ghate & Lele (2017)) which for this problem, is a known analytical function of z.

Figure 21 shows the two inputs used for Gabor mode enrichment of the coarse simulation data. While all three coarse representations largely agree in the prediction of the length scale measure, L_{iso}, it is clear that the shearing constant seen in AMD64 and AMD128 (to a lesser extent) is lower that what is expected from ideal filtering. This lower value of the shearing parameter results in enrichment of subfilter scales that are more isotropic than those expected by the implied grid filtering in coarser simulations for $z/H < 0.2$ as is discussed in a subsequent section.

Figure 22 and 23 show the single-point and two-point (1D spectra) correlations for the Gabor mode enriched AMD128 case. The single point correlations suggest that for $z/H > 0.3$ the Gabor modes accurately represent the second order statistics of the subfilter scale turbulence. This is supported by the various 1D spectra shown for all three components in Figure 22a at $z/H = 0.4$ where a consistent wavenumber extrapolation of each spectrum is observed. For $z/H < 0.2$, while the single point correlations show overprediction of variances, we note that the 1D spectra suggest that this overprediction is primarily due to overprediction of the energy in low (resolved-scale) wavenumbers for the coarse simulation (see Figure 22b). This is especially evident in the wall-normal velocity which appears to suffer from large aliasing at the $z = 0.05H$ location. The turbulent kinetic energy profiles for both AMD128 and AMD64 are shown in Figure 24. The figure shows that enrichment of both AMD128 and AMD64 recovers the total resolved turbulent kinetic energy of the reference simulation to a reasonable degree of accuracy at

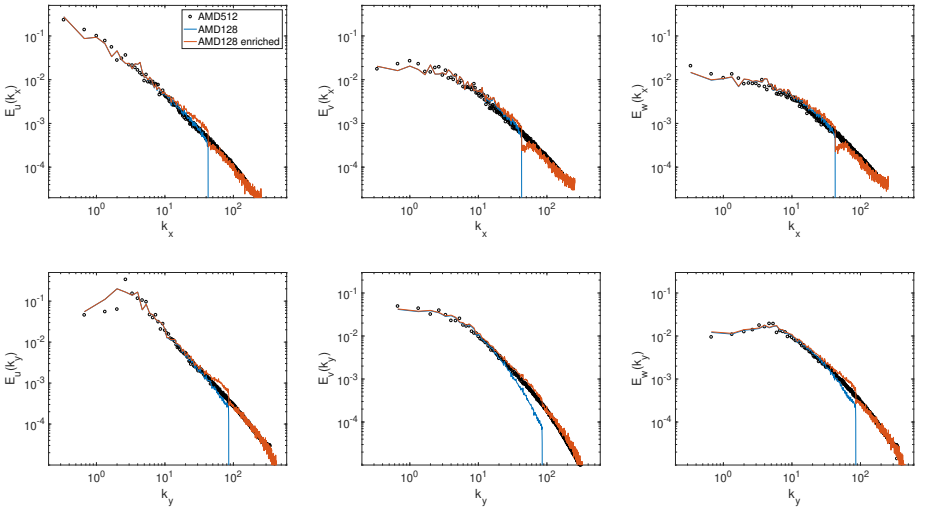

(a) $z = 0.40H$

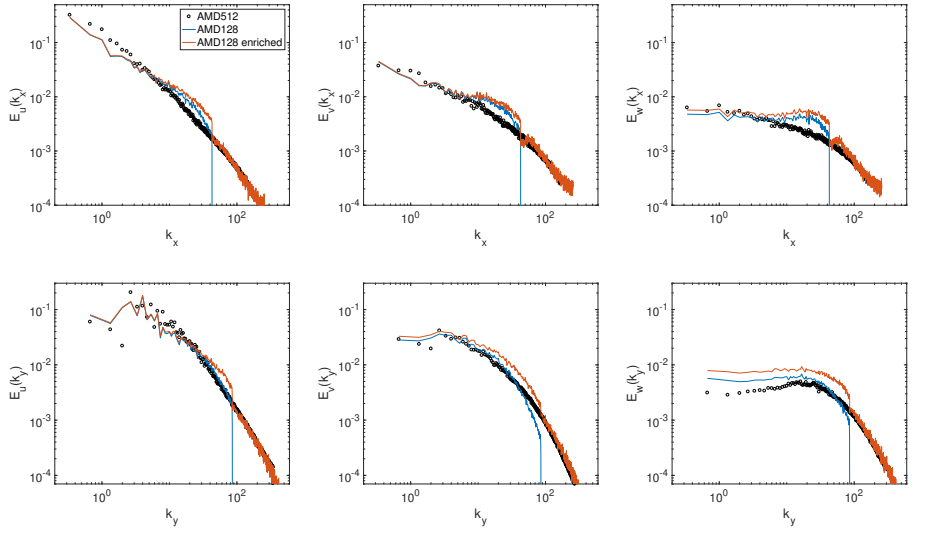

(b) $z = 0.05H$

FIGURE 23. Velocity power spectra for Gabor mode enriched `AMD128` LES

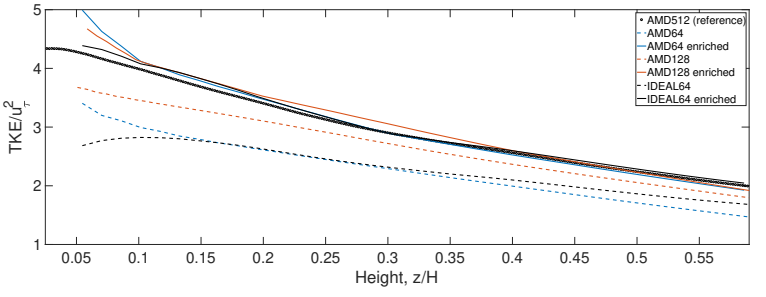

FIGURE 24. Mean profiles of turbulent kinetic energy (TKE)

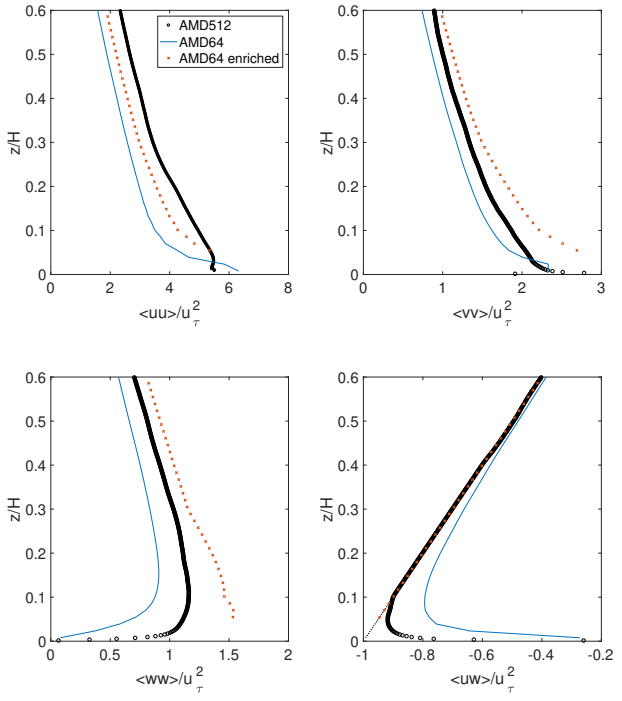

FIGURE 25. Single point correlations as a function of height for the AMD64 case enriched using Gabor modes.

virtually all wall-normal locations. Furthermore, while some discrepancies exist between AMD64 and IDEAL64 for $z/H < 0.15$, it is promising to note that the post-enrichment total TKE in the a-posteriori setting (AMD SGS model) is similar to the TKE in the a-priori setting (idealized filtering of reference simulation).

We now consider the single point correlations for the AMD64 case in Figure 25. The three variance profiles suggest that although the total subfilter TKE is reasonably accurate, the contributions of each of the three components has a qualitative bias at all wall normal distances; the streamwise variance is underpredicted at the expense of substantial overprediction in the spanwise and wall-normal variances. In order to further explore this deficiency, we now consider the 1D spectra for the three velocity components in Figure 26. All size 1D spectra considered at the two wall normal locations indicate that virtually all the error in single point correlations is a consequence of errors in the low-wavenumber region which is expected to be resolved by the coarse grid LES. We will refer to this flaw observed in the 64-point simulations as *overenrichment* and the following subsection discusses this aspect of a-posteriori enrichment. Enrichment of IDEAL64 case (shown in Figure 27 and Figure 28) is used to explain this overenrichment in the a-posteriori (AMD64) case.

5.3. *Over-enrichment in coarse LES*

The overall quality of the Gabor model enrichment for AMD64 can be broadly summarized using the following four observations.

(i) Significant underprediction of streamwise variances through the bulk of the boundary layer, particularly above $z/H > 0.1$. The 1D spectra of u at $z = 0.4H$ (see Figure 26b) confirm that this is entirely due to missing energy in the $k_x L_x/(2\pi) \approx 2$ and

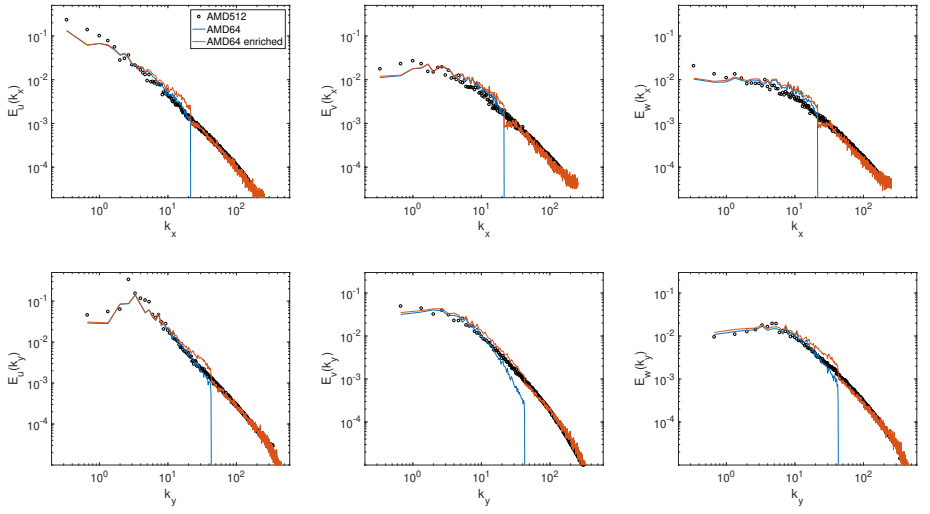

(a) $z = 0.40H$

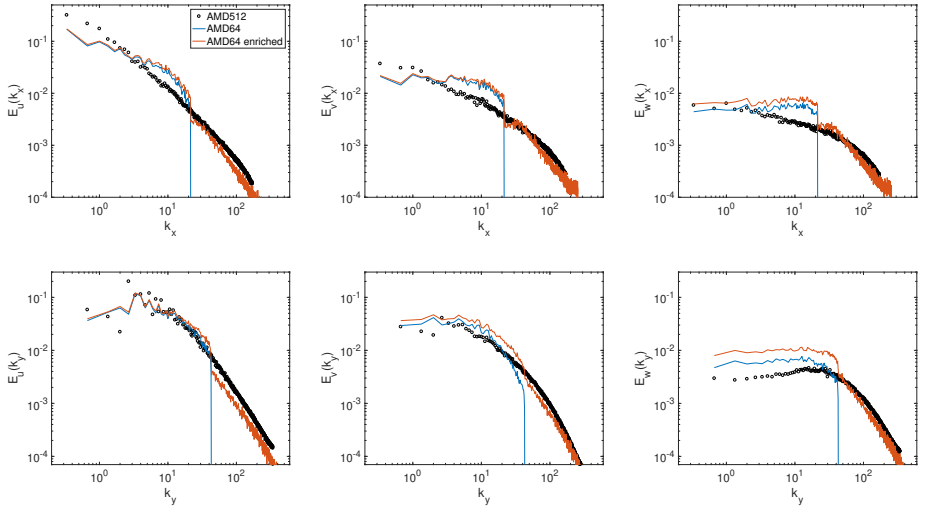

(b) $z = 0.054H$

FIGURE 26. Velocity power spectra for Gabor mode enriched `AMD64` LES

$k_y L_y/(2\pi) \approx 4$ coherent streak that was briefly discussed earlier. Since the present application is a one-way-coupled enrichment, Gabor mode enrichment simply cannot alleviate this deficiency of coarse simulations because it pertains to large wavelength meandering motions. For the `IDEAL64` case, the filtering procedure does not remove any energy from this large streamwise coherent structure and as a result Gabor mode enrichment performs remarkably well as shown in Figures 27 and 28. In other words, the profiles of the resolved Reynolds stress, $< u'w' >$ for `AMD64` suggest that for $z > 0.2H$, the subfilter scales are primarily isotropic. However, the profiles for the streamwise velocity variances are inconsistent with this characterization of subfilter scales primarily due to the underprediction of the single-point correlation $< u'u' >$ associated with the large coherent streak.

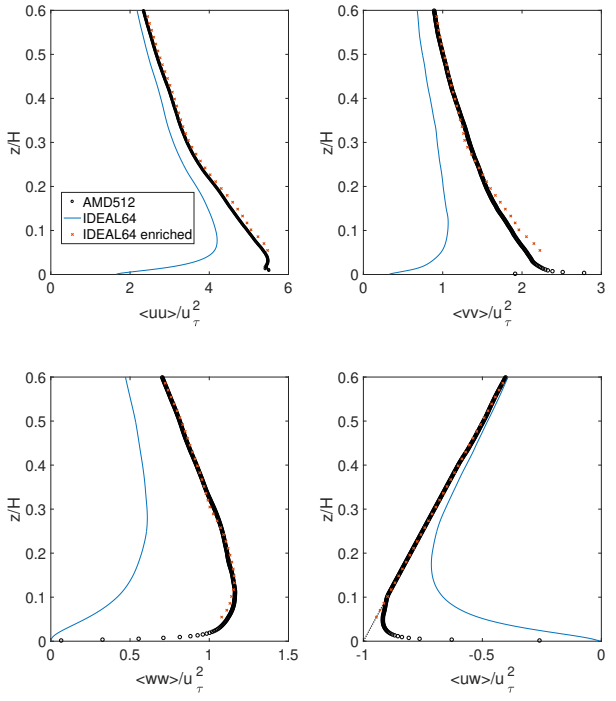

FIGURE 27. Single point correlations as a function of height for the `IDEAL64` case enriched using Gabor modes.

(ii) The low dissipation property of AMD model results in substantially more energy at barely resolved scales near its Nyquist limit, which is suggestive of aliasing. This is particularly evident in the k_y spectrum of spanwise and wall normal velocity fluctuations, and also results in substantial overprediction of the Reynolds stress $< u'w' >$. This results in an overenrichment of the wall-normal velocity component when the variance of the enriched field is compared with the higher resolution simulation. This is in contrast to our observations for simulations done using the wall-damped Smagorinsky model (discussed in Ghate (2018)) which is overly dissipative near the wall and consequently underpredicts the Reynolds stress, which results in Gabor mode enrichment of highly anisotropic small scales (seen in terms of large c_τ value) near the wall.

(iii) The turbulent kinetic energy spectra at $z/H = 0.05$ and $z/H = 0.40$ are shown in Figure 29. Following Figure 29, we note that the gradual decay in energy for values around the cutoff wavenumber (Nyquist wavenumber for coarse simulations), is due to anisotropy of the grid resolution ($dx = 2dy$) and not due to excessively dissipative numerics or SGS modeling. At the $z/H = 0.05$ plane, the `LES512` shows a prominent k^{-1} energy scaling at low wavenumbers suggestive of production scales. However, it is apparent that the transition from k^{-1} to $k^{-5/3}$ is not quite well resolved, which suggests that perhaps the `AMD512` LES used for reference is not sufficiently well resolved at $z/H = 0.05$. The primary purpose of showing the TKE spectrum along with the 1D velocity spectra is to emphasize that if we evaluate solution quality using the TKE and its scale distribution, Gabor mode enrichment seems to work rather well. This is consistent with the basic philosophy of eddy viscosity type SGS modeling which attempts to correctly model the TKE cascade, but is not necessarily designed for accuracy in representing the spectral anisotropy. These results make a strong case for the future work towards improving SGS

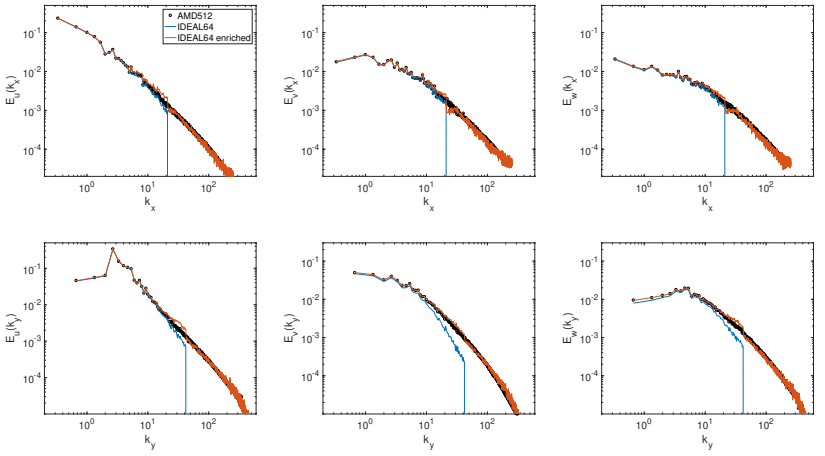

(a) $z = 0.40H$

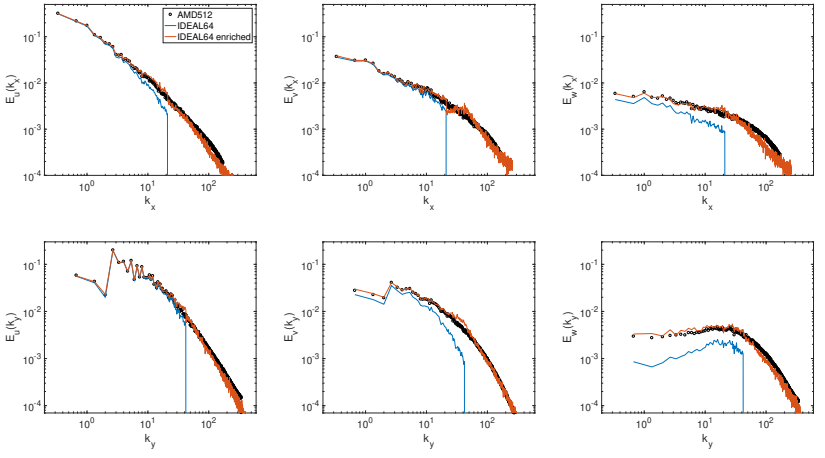

(b) $z = 0.054H$

FIGURE 28. Velocity power spectra for Gabor mode enriched `IDEAL64` LES

modeling to improve representation of anisotropic effects in very coarse simulations of wall bounded turbulence.

(iv) Figure 20a suggests that `AMD128` does not suffer from severe underprediction of energy in the large spanwise coherent structure, like the $192 \times 192 \times 64$ simulations. However, Figure 20d indicates that the increase in grid points does not remove the over-prediction in Reynolds stress ($< u'w' >$) near the wall; in fact, the resolved Reynolds stress also increases as the grid is refined from `AMD64` to `AMD128`. It is clear that while overshoots in spanwise and vertical velocity variances still persist (over prediction of resolved Reynolds stress by `AMD128` requires enriched scales to be more isotropic than true subfilter scales), the underprediction of single point correlations for $z > 0.2H$ is not present anymore. Further work is needed to study the failure of SGS models at predicting the correct resolved near wall anisotropy in the asymptotic Reynolds number limit ($Re \to \infty$).

Again, it is important to emphasize that while the single point correlation profiles in Figures 25 suggest limited success in Gabor mode enrichment of the flow studied in this

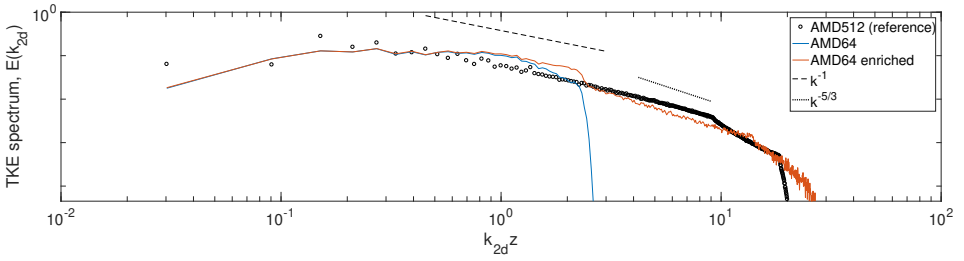

(a) $z = 0.054H$

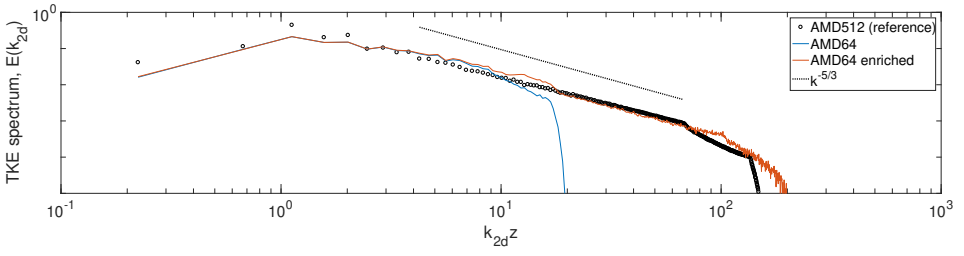

(b) $z = 0.40H$

FIGURE 29. Turbulent kinetic energy spectrum using polar wavenumber, $k_{2d} = \sqrt{k_x^2 + k_y^2}$. The TKE spectrum has been defined (and normalized) such that $\frac{<u_i u_i>}{2}(z) = \int_0^\infty E(k_{2d}) dk_{2d}$.

section, the analysis using 1D spectra suggests otherwise. Even though the two-point statistics of the large scales predicted using the three SGS models have some deficiencies, the enrichment procedure does embed small scales that are fairly representative of the true subfilter scales. Much of this is attributed to informed choice of using an input length scale (L_{iso}) measure computed using spanwise velocity fluctuations instead of streamwise fluctuations.

6. Conclusions

The turbulence enrichment approach using spatially and spectrally localized *Gabor modes* introduced by Ghate & Lele (2017) is significantly developed and extended in this work. We formally define the turbulence enrichment problem to be the one where subfilter scales are superposed on large scales resolved on coarse-grid LES where the subfilter-scales exhibit the following properties: a) consistent extrapolation of second order spectra and two-point spatial correlations for spatially inhomogeneous turbulence, b) representation of spatially localized and intermittent inter-scale energy transfer from large to small scales, and c) accurate characterization of physics responsible for temporal decorrelation of the enriched scales. Under an assumption of local *quasi-homogeneity* of near-filter scales, Gabor wavepackets/modes provide an optimal basis for representation of solenoidal velocity scales that can represent a physically consistent and realizable structural anisotropy. They enable significant compression in degrees of freedom needed for representation of subfilter-scale turbulence. Furthermore, by using WKB arguments, the temporal evolution of these small scales is expressed via simple ordinary differential equations for each Gabor mode. The rendering algorithm (see Appendix B) shows that the velocity fields can be computed in physical space on finer numerical grids using an efficient Non-Uniform Fast Fourier Transform (NUFFT). Rendering can either be done at point locations or a subset of the physical domain without having to evaluate the

fields in the entire domain at each simulation time step. This computational efficiency of the algorithm can facilitate its use in applications beyond LES enrichment such as inflow generation as was done recently in Ghate *et al.* (2020).

We investigate the accuracy of the enrichment algorithm for two LES problems in an *a-posteriori* setting. In the first problem forced homogeneous isotropic turbulence (HIT) is studied and the analysis shows that the enrichment not only provides an accurate scale-space extrapolation of the coarse LES, but also captures the inter-scale transfer of energy very accurately. The small scales represented by Gabor modes can be interpreted as velocities induced by a set of Burgers-Townsend vortices dispersed within *quasi-homogeneous* regions with their orientations defined by the gradients of the larger scales. The second problem considers rough wall boundary layer at large Reynolds number in a half-channel configuration. Two deficiencies relating to aliasing of vertical velocity (near walls) and under-prediction of energy in large streamwise structures by coarse grid LES using conventional SGS models are identified. Despite these deficiencies of the original LES model, the enrichment leads to promising results, especially when enrichment is characterized by the increase in turbulent kinetic energy. We argue that accurate differentiation of *physical anisotropy* associated by Reynolds stress transport and the *geometric anisotropy* associated with the grid-filtering is needed by the enrichment algorithm in order to provide correct variances for the enriched fields. Future development of this enrichment approach will focus on applications to non-equilibrium flows, analysis of subfilter-scale enriched pressure and analysis of higher order moments implied in the enrichment.

Acknowledgements

ASG was funded by Tomkat Center for Sustainable Energy at Stanford University. SKL acknowledges partial support from NSF-CBET-1803378. All simulations were performed on Stampede2 supercomputer under the XSEDE project ATM170028. The authors would also like to thank the anonymous referees for their thoughtful comments and contribution to this work.

Declaration of Interests

The authors report no conflict of interest.

Appendix A: Choice of scale separation parameter, ε and error in divergence

One of the consequences of velocity field evaluation using Equation 3.8, is that the synthesized velocity field is not exactly divergence free since the gradient of the cosine support function is not orthogonal to the induced velocity vector. It is easy to see that the true divergence is $\mathcal{O}(\varepsilon)$, which provides an interesting opportunity to study the impact of the scale separation parameter, ε. However, note that the velocity field synthesized can in fact be projected onto an exact divergence free basis at negligible extra computational cost, since we can simply project each of the contributions in Equation 3.8 individually/locally using Fast Fourier Transforms in the support region (regardless

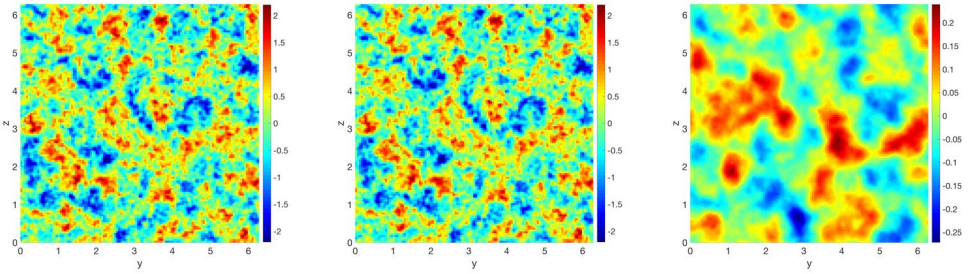

(a) u_A, evaluated using Eq. 3.8 (b) u_B, evaluated using Eq. 1 (c) Difference, $u_A - u_B$

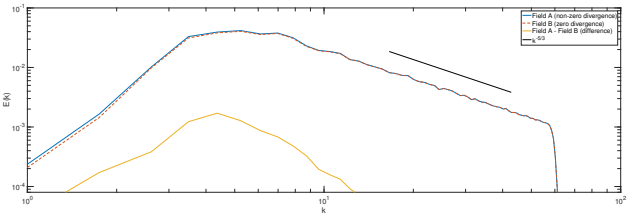

(d) Kinetic energy spectrum

FIGURE 30. Divergence errors when $\varepsilon = 0.25$. Percentage decrease in KE due to projection: 1.5%.

of the global boundary conditions), thereby replacing Equation 3.8 with:

$$\boldsymbol{u}(\boldsymbol{x}) = \sum_{i=1}^{N_b} \boldsymbol{u}^{\perp}(\boldsymbol{x}, \boldsymbol{x}_0^{(i)}) \quad ; \quad \boldsymbol{u}^{\perp}(\boldsymbol{x}, \boldsymbol{x}_0^{(i)}) = \texttt{ifft}\left\{ \left(\delta_{ij} - \frac{K_i K_j}{K_m K_m} \right) \cdot \texttt{fft}\left\{ \boldsymbol{u}(\boldsymbol{x}, \boldsymbol{x}_0^{(i)}) \right\} \right\} \tag{1}$$

where the upper case K_i is used to denote equispaced wavenumbers corresponding to the support of the quasi-homogeneous region†. Figures 30 and 31 show the impact of this exact divergence projection on the induced field, for an example, synthesis of isotropic turbulence for two choices of the scale separation parameter, ε, taken as 0.25 and 0.0625. The $\varepsilon = 0.25$ case corresponds to enrichment used throughout this paper, while the $\varepsilon = 0.0625$ is generated by setting $(\Delta_{QHx}, \Delta_{QHy}, \Delta_{QHz}) = (8\Delta_x, 8\Delta_y, 8\Delta_z)$. In practice this is interpreted as the resolution of LES increased by a factor of 4 in each direction. These results show that a reduction of ε by a factor of 4 results in reduction in divergence error. Furthermore, the loss in KE due to production is essentially negligible. However, recall that this reduction in ε comes at a loss of spatial localization since the support function is four times as wide as the theoretical minimum. The comparison of the energy spectra further shows that the impact of this exact projection (Equation 1) is rather negligible in terms of the overall energy even for the $\varepsilon = 0.25$ case. Comparison of two-point correlations between the two fields also suggests negligible impact of the local projection. This is an excellent prospect since it suggests that we can avoid the additional projection and thereby evaluate the fields directly at the required location as opposed to evaluating them on a Cartesian mesh, $\boldsymbol{x}$. For example, for an application involving arbitrary located particles at $\boldsymbol{x}_p$,the sum in Equation 3.8 can again be computed using a Type III NUFFT if a direct evaluation is prohibitively expensive.

† In practice one needs to deal with the odd-ball wavenumber before using the projection in Equation 1

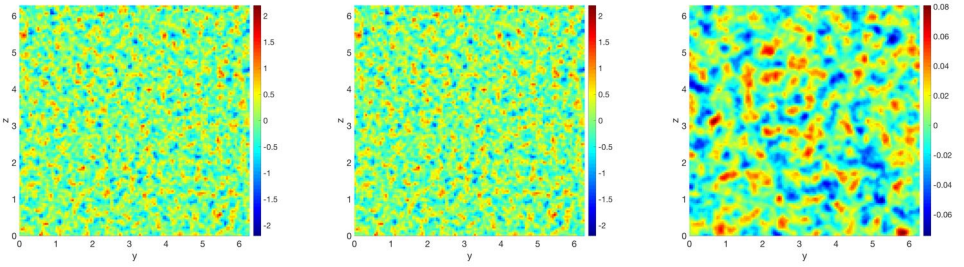

(a) u_A, evaluated using Eq. 3.8 (b) u_B, evaluated using Eq. 1 (c) Difference, $u_A - u_B$

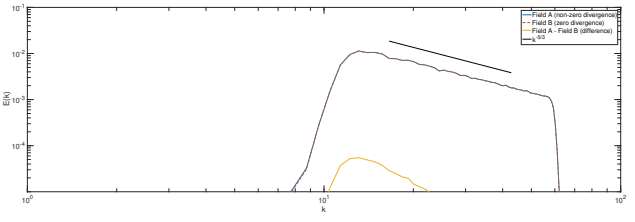

(d) Kinetic energy spectrum

FIGURE 31. Divergence errors when $\varepsilon = 0.0625$. Percentage decrease in KE due to projection: 0.25%.

Appendix B: Fast rendering algorithm using Non-uniform FFTs

The overall algorithm discussed in this appendix relies on the Gabor mode description shown in Figure 4. This illustration leads to the following three key observations: (a) The Gabor modes within each *Quasi-homogeneous* region affect the flow within the Quasi-homogeneous region, and a portion of the immediately adjacent Quasi-homogeneous regions, (b) The velocity field at each location in physical space is a superposition of contributions from 8 Quasi-homogeneous regions in 3D space, and (c) The Gabor modes advect in time similar to passive tracers, or non-inertial particles. This means at two different times, the set of modes in a specific QH region changes with time.

Hybrid MPI+X rendering

Since most modern computational many-core architectures strongly favor, an MPI+X paradigm, we first identify the tasks necessary in an MPI formulation (Single Program, Multiple Data).

(i) Mode transfer - *Latency bound*, can be done using non-blocking, point-to-point communicators.

(ii) Gabor Transform - *Bandwidth bound*, can be done using non-blocking, point-to-point communicators.

Further note that the implementation of the purely MPI code is trivial and requires the use of halo-region exchanges (accomplished here using non-blocking point-to-point communicators) and particle/mode exchanges also requiring non-blocking point to point communicators. However, the halo-cell exchanges (physical space induced velocities) are a substantial bottle neck since each overlap in Region-of-influence consists of around 8-16 points (along each direction). This communication cost scales linearly with surface area of processor decompositions. Therefore, there appears to be a substantial advantage of reducing the total number of MPI processes spawned during execution, and hence the choice to pursue a hybrid MPI + OpenMP implementation was made. The shared

memory aspect of the parallelization (OpenMP) requires substantial modifications to a serial implementation of the enrichment algorithm due to the multitude of race conditions that occur in both the Gabor transform, and the particle evolutions phases. The focus of the rest of this appendix hence will be limited to this shared memory portion of this implementation. The distributed memory aspects are identical to solutions to PDEs using finite difference schemes; i.e. it requires neighbor halo-exchanges for the Eulerian data, as well as neighbor point-to-point communications for any Gabor mode exchanges. All MPI calls are made by a single thread (`OMP SINGLE` directive is used to identify the thread).

The overall enrichment algorithm

The overall shared memory algorithm can be decomposed into the following set of steps.

(i) **Initialization/seeding of random modes in each QH region.** This is done by simply distributing the QH regions among threads for the portion of the domain represented by each MPI process. Thread and process independent seeds are used to ensure reproducibility of the stochastic initialization.

(ii) **Rendering** (Transform from Gabor modes to physical space fields) This is performed by modifying the Greengard & Lee (2004) Non-Uniform Fast Fourier Transform (NUFFT) algorithm.

(iii) **Particle evolution**. Since the particles within each QH region evolve due to the large scale gradients within that QH region, this portion of the particle evolution is trivial to perform using multiple threads. However, the particles also advect to regions outside their original QH regions, and hence require to be resorted/histrogramming. While this process can be performed using multiple threads special attention is needed to avoid the ensuing race conditions.

Gabor Transform/Rendering using OpenMP

The Gabor tranform from a set of m modes to the uniform mesh in physical space can be expressed as two successive steps

(i) Gaussian gridding (convolution): This step is operationally $\mathcal{O}(m)$

(ii) 3D Fast Fourier Transform: This step is operationally $\mathcal{O}(\tilde{N}^3 \log_2(\tilde{N}))$ where $\tilde{N}$ is an upsampled mesh depending on the desired precision. For present applications, 10^{-9} precision requires twice-upsampling and as such, this FFT operation is approximately 8 times as expensive as a regular FFT. That is, the FFT portion of an NUFFT to N grid points has an operational complexity of $\mathcal{O}(8N^3 \log_2(N))$.

Since each grid point is influenced by Gabor modes in 8 QH regions, the NUFFT cannot be performed simultaneously in adjacent QH regions due to the implied race conditions. To overcome this limitation (and to speed up the NUFFT), a further decomposition is made in wavespace k for each QH region (see Figure 32). Since the contribution due to large k values requires a high resolution mesh, we cannot compute and store the field generated by each QH region in a temporary buffer (1 buffer for each QH region would require memory 8 times larger than the problem size since window support is a factor of 2 larger than QH region in each direction). However, we again leverage the logarithmic sampling in $k-$space as shown in Figure 32. The calculation of the NUFFT is now performed in three stages:

(i) The NUFFT from the low k modes is evaluated on a coarse mesh spanning the entire Region of influence (RoI or support of the window), this operation typically uses about 85% of the modes within the QH region. This data can be represented on a coarser mesh (see figure 33a/b, bottom pane), so it is stored in memory for each QH region separately. This operation uses a single NUFFT call.

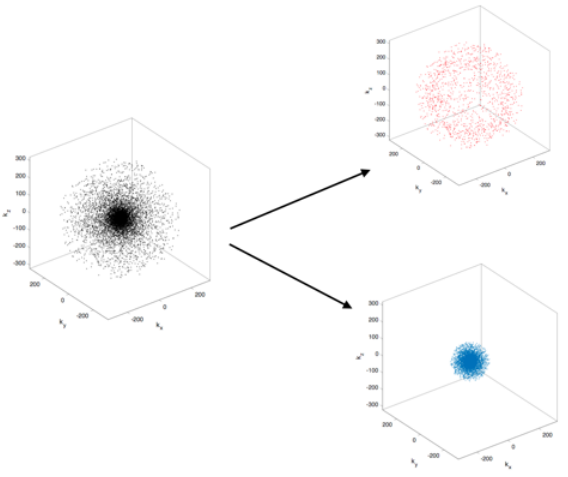

FIGURE 32. Prep stage: The modes in each QH region are decomposed into large shells and small shells based on a cut off wavenumber, k_{abs}. In our application this decomposition ratio results in approximately $7:1$ in number of modes in each category. If m modes are present, this operation does NOT require a sorting operation; instead it is performed using m conditional statements and copies and as such the complexity is $\mathcal{O}(m)$ which is lower than that of `quicksort`.

(ii) The RoI surrounding a QH region is decomposed into $4 \times 4 \times 4$ subdomains (QH region into $2 \times 2 \times 2$ octants), and the tranform from large k to each one of these octants is computed recursively. There are two algorithms implemented for this transform: a) Naive NUFFT (Figure B.3a) and b) Partial NUFFT (Figure B.3b). Depending on the application and the CPU architecture, the Partial NUFFT algorithm can be 4-5 times faster than the Naive algorithm due to substantially higher arithmetic intensity and the use of Level 2 BLAS call (`DGEMV/SGEMV`). The data from the coarse grid (step 1), low k mode is oversampled within each octant sequentially. The resulting race conditions between threads are prevented by using $4 \times 4 \times 4$ OpenMP barrier calls. Finally note that at this stage, the code does not perform any interpolation from step 1 data; instead it simply stores the higher resolution grid data obtained at the end of the NUFFT since the NUFFT call anyway uses a twice upsampled grid for the FFT. As a consequence it requires at least 8 times more memory than the number of degrees of freedoms; future implementations can address this by performing explicit interpolation using cubic splines.

Finally, note that for the compression ratios typically seen in applications (> 85) the cost is almost entirely given by the FFT stage of the NUFFT performed in step 2. Cost of Step 1 is approximately a factor of 6-8 smaller than that of step 2. Now since the NUFFT in step 2 is performed on a twice over-sampled mesh, our numerical experiments show that the **cost of NUFFT using m modes on N grid points is approximately 10 times larger than the cost of computing a single 3D FFT on N grid points** for $m \ll N$.

Computational cost of the overall algorithm

Finally, let's return to the HIT enrichment example to illustrate the overall operational count of the enrichment algorithm. We will consider the HIT enrichment example studied in Section 5.1.

- LES problem size, $N_{\texttt{LES}} = 32^3$
- Number of quasi-homogeneous regions, $N_{\texttt{QH}} = 16^3$.
- Number of Gabor modes per QH region, $m = 512$

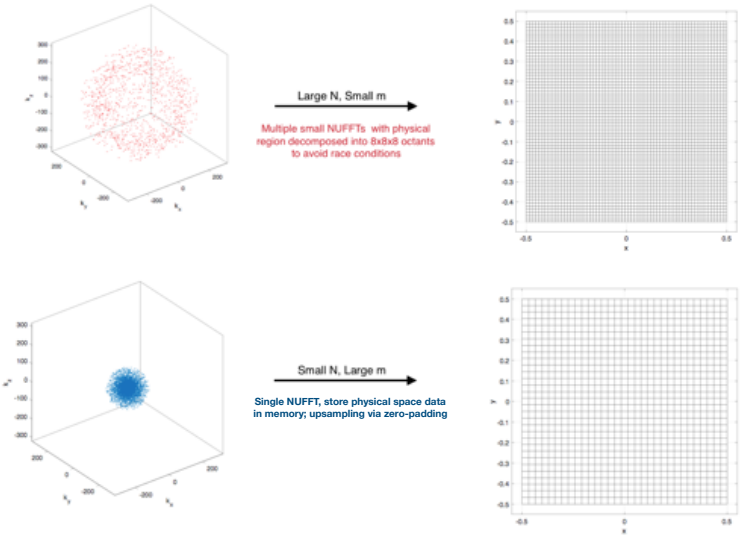

(a) *Naive NUFFT algorithm*

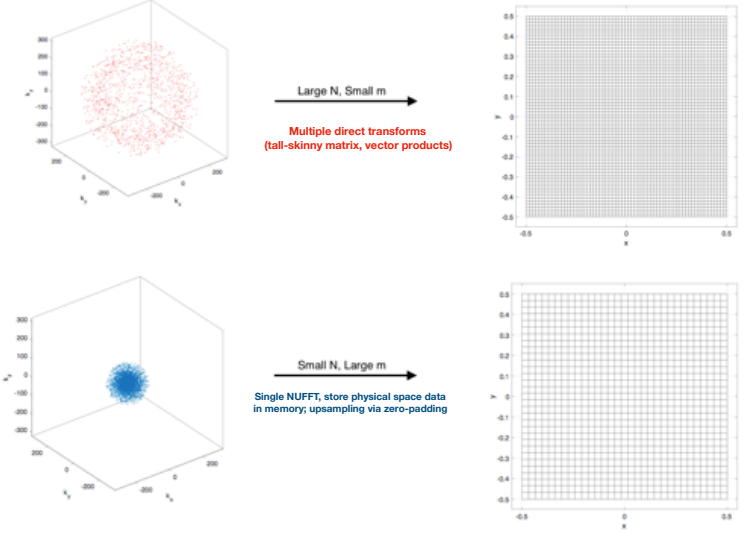

(b) *Partial NUFFT algorithm*

FIGURE 33. Compute stage: Each subset of Gabor modes is transformed separately on a different set of physical grids. This is done in order to reduce *race conditions* in the OpenMP portion of the calculations, and also for improved efficiency (in case of the partial NUFFT algorithm).

- Number of grid points to represent the enriched fields, $N = 256^3$
- Compression in DOF: $(1 - \frac{N_{\mathtt{QH}} \times m}{N}) \times 100 = 15\%$ (can do better by reducing m or increasing N).
- Number of grid points within RoI for each QH region, $N_{\mathtt{RoI}} = 2^3 \frac{N}{N_{\mathtt{QH}}} = 32^3$ since RoI is twice as wide as QH region.

- Total number of NUFFTs needed: $N_{\texttt{QH}} = 16^3$
- Cost per NUFFT:
  - **Naive NUFFT algorithm**: Cost per transform is $\mathcal{O}(\lambda N_{\texttt{RoI}} \log_2(N_{\texttt{RoI}}^{1/3}))$, where λ is the ratio of cost of FFT to cost of NUFFT and is approximately 10 for the present application where $m/N_{\texttt{RoI}} = 0.0156$. Total cost of transforming each field from Gabor modes to the entire domain: $(\lambda N_{QH}) \times \mathcal{O}\left(N_{\texttt{RoI}} \log_2(N_{\texttt{RoI}}^{1/3})\right)$. This corresponds to $\lambda N_{\texttt{QH}}$ many $N_{\texttt{RoI}}$ sized 3D FFTs.
  - **Partial NUFFT algorithm**: Cost per transform is $\mathcal{O}(\frac{\lambda}{8} N_{\texttt{RoI}} \log_2(N_{\texttt{RoI}}^{1/3}) + m N_{\texttt{RoI}})$ where the first term is the NUFFT for coarse grid and the second term is a direct transform for the fine grid. Total cost of transforming each field from Gabor modes to the entire domain: $(\frac{\lambda}{8} N_{QH}) \times \mathcal{O}\left(N_{\texttt{RoI}}(\log_2(N_{\texttt{RoI}}^{1/3}) + \frac{8m}{\lambda})\right)$. Given $\lambda/8 \approx 1$ this cost can be interpreted primarily as $N_{\texttt{QH}}$ many $N_{\texttt{RoI}}$ sized 3D FFTs, followed by $N_{\texttt{RoI}}$ many $m \times N_{\texttt{QH}}$ sized matrix vector products.

Operationally, λ depends on the choice of the library used for FFT portion of the NUFFT, and our numerical experiments suggest $\lambda \approx 11$ for `FFTW` and $\lambda \approx 9$ for `fftpack`. Using the **naive NUFFT algorithm**, the cost of a serial calculation of the Gabor mode velocities on a 256^3 mesh is approximately equivalent to the cost of performing **35** 3D FFTs of size 256^3 using the FFTW library with AVX2 vectorization. Using the **partial NUFFT algorithm**, the cost of a serial calculation of the Gabor mode velocities on a 256^3 mesh is approximately equivalent to the cost of performing **8** 3D FFTs of size 256^3 using the FFTW library with AVX2 vectorization.

Note that this calculation does not indicate the total cost of simulation using Gabor modes. The bulk of the cost reduction using Gabor modes lies in the temporal evolution description via a set of ODEs and as such this transform needs to be performed only when the fields need to be evaluated in physical space. Furthermore, the algorithm allows for the transform to be performed locally; only physical regions of the domain that need finer scale information need to use the transform.

In this worst case scenario, where the subfilter scales are needed in the entire domain at each small scale time step, this factor of 35 for the cost of a single transform from Gabor modes to physical space is still substantially smaller than evaluation of the full equations using conventional methods where just an iterative Poisson solver typically requires $\mathcal{O}(1000N)$ operations per time step (assuming RK substeps) for incompressible flows evaluations.

Appendix C: Temporal evolution equation for a Gabor mode

In order to derive the Gabor mode evolution equation we make the following arguments regarding the superfilter fields. Given a quasi-homogeneous region, $x \in \mathcal{D}(\boldsymbol{x}_0)$ and a corresponding time scale, τ

- The superfilter field, $U_i(x_i)$ is expanded in space as

$$U_i(x_i) = U_i^0 + x_j \, \partial_j U_i|^0 \quad , \quad x \in \mathcal{D}(\boldsymbol{x}_0)$$

- Galilean transform to the *sweeping frame*:

$$\tilde{x}_i = x_i - U_i^0 t \quad , \quad t \in [0, \tau]$$

Consider the evolution of subfilter scales (Eq. 2.8) in the *sweeping frame*,

$$\partial_t u_i + (x_m \partial_m U_j)\partial_j u_i = -u_j \partial_j U_i - \partial_i p + \partial_j h_{ij} + \frac{1}{\mathrm{Re}} \partial_j \partial_j u_i + \partial_j \tau_{ij} \tag{1}$$

where h_{ij} is the stress associated with non-local (quadratic) interactions, $h_{ij} = -(u_i u_j + U_i^r u_j + u_i U_j^r)$. Next, by assuming Gabor modes of the form for an arbitrary function, $f(\boldsymbol{x}, t)$:

$$f(\boldsymbol{x}, t) = \sum \hat{f}(\boldsymbol{x}_0, t, \varepsilon) e^{i(\boldsymbol{k}(t)\cdot\boldsymbol{x})} \tag{2}$$

where the $\hat{f}(\boldsymbol{x}_0, t)$ is the complex amplitude ($\boldsymbol{x}_0$ is a coordinate fixed with the large scales; $d\boldsymbol{x}_0/dt = U(\boldsymbol{x}_0)$) with the spatial windowing corresponding to a scale separation ratio, ε. Thus, for an arbitrary function, we have

$$\partial_j f(\boldsymbol{x}, t) = \sum \left(i k_j(t) \hat{f}(\boldsymbol{x}_0, t, \varepsilon) \right) e^{i(\boldsymbol{k}(t)\cdot\boldsymbol{x})} + \mathcal{O}(\varepsilon)$$

We will use this identity to substitute the modes (Equation 2) into the governing equation for small scales (Equation 1). However, we will first derive the eikonal equation which describes the temporal evolution of wavenumbers, $\boldsymbol{k}(t)$. Consider an arbitrary (passive) scalar field, $\phi(\boldsymbol{x}, t)$ advected by the large scale field, $\boldsymbol{U}(\boldsymbol{x}, t)$. That is, the scalar field $\phi(\boldsymbol{x}, t)$ satisfies

$$\frac{D\phi}{Dt} = \partial_t \phi + U_j \partial_j \phi = 0 \tag{3}$$

Now, assuming a modal representation of the field at time, $t = 0$ of the form:

$$\phi(\boldsymbol{x}, t = 0) = \hat{\phi}(\boldsymbol{x}_0, \varepsilon) e^{i\boldsymbol{k}\cdot\boldsymbol{x}} \tag{4}$$

the Eikonal equation can be obtained by postulating that the temporal evolution of the field, $\phi(\boldsymbol{x}, t)$ can be obtained by a constant (in time) amplitude $\hat{\phi}$ (in the frame of $\boldsymbol{x}_0$) and time dependent wavenumber, $\boldsymbol{k}(t)$. Simple substitution of Equation 4 into Equation 3 and using the properties: $U_i(\boldsymbol{x}, t) = U_i(\boldsymbol{x} = 0) + \partial_j U_i (x_j - x_j^0)$ (quasi-homogeneity) and the definition $d\boldsymbol{x}_0/dt = \boldsymbol{U}(\boldsymbol{x}_0)$ we get,

$$\frac{D\phi}{Dt} = i\hat{\phi}(\boldsymbol{x}_0) x_j \left(\frac{dk_j}{dt} + k_m \frac{\partial U_m}{\partial x_j} \right) = 0 \tag{5}$$

Due to the arbitrary nature of ϕ, we now have the Eikonal equation for $\boldsymbol{k}(t)$:

$$\partial_t k_j + k_m \partial_j U_m = 0 \tag{6}$$

Using this evolution equation for the wavenumbers, we can show that the Gabor mode representation of the left hand sides of Equation 1 is given as:

$$\partial_t u_i + (x_m \partial_m U_j) \partial_j u_i = e^{i\boldsymbol{k}(t)\cdot\boldsymbol{x}} \partial_t \hat{\boldsymbol{u}}(\boldsymbol{x}_0, t, \varepsilon) + \mathcal{O}(\varepsilon) \tag{7}$$

Now, consider the straining terms that appear on the right hand side of Equation 1. The Gabor mode representation of the straining terms (using Quasi-homogeneneity assumptions) is simply:

$$\widehat{u_j \partial_j U_i} = \hat{u}_j(\boldsymbol{x}_0, t, \varepsilon) \partial_j U_i(\boldsymbol{x}_0, t) \tag{8}$$

Substituting these definitions in Equation 1, we get

$$\partial_t \hat{u}_i = -\hat{u}_j \partial_j U_i - i k_i \hat{p} + i k_j \hat{h}_{ij} + \frac{1}{\mathrm{Re}} \partial_j \partial_j \hat{u}_i + i k_j \hat{\tau}_{ij} \tag{9}$$

The pressure term can be eliminated by multiplying Equation 9 by the projection tensor, $\left(\delta_{im} - \frac{k_i k_m}{k_l k_l} \right)$ and noting that:

$$\left(\delta_{im} - \frac{k_i k_m}{k_l k_l} \right) (i k_i \hat{p}) = i k_m \hat{p} - i k_m \hat{p} = 0 \tag{10}$$

Upon projection (and using the property $k_m \hat{u}_m = \mathcal{O}(\varepsilon)$), the left hand side of Equation 9 simplifies to

$$\partial_t \hat{u}_m - \frac{k_i k_m}{k_l k_l} \partial_t \hat{u}_i = \partial_t \hat{u}_m - \left(-\frac{\hat{u}_i}{k_l k_l} \partial_t (k_i k_m) \right) + \mathcal{O}(\varepsilon) = \partial_t \hat{u}_m - \left(-\frac{k_m \hat{u}_i}{k_l k_l} \partial_t (k_i) \right) + \mathcal{O}(\varepsilon) \tag{11}$$

Now using the Eikonal equation 6, we get:

$$\left(\delta_{im} - \frac{k_i k_m}{k_l k_l} \right) \partial_t \hat{u}_i = \partial_t \hat{u}_m - \left(\frac{k_m k_p}{k_l k_l} \right) (\hat{u}_i \partial_i U_p) + \mathcal{O}(\varepsilon) \tag{12}$$

Similarly, the straining term projects as

$$\left(\delta_{im} - \frac{k_i k_m}{k_l k_l} \right) (-\hat{u}_j \partial_j U_i) = -\hat{u}_j \partial_j U_m + \left(\frac{k_m k_i}{k_l k_l} \right) (\hat{u}_j \partial_j U_i) \tag{13}$$

Substituting Equations 12 and 13 into Equation 9, we get

$$\partial_t \hat{u}_m \;=\; -\hat{u}_k \partial_k U_j \left(\delta_{mj} - 2 \frac{k_m k_j}{k_l k_l} \right) + i k_j \hat{h}^{\perp}_{mj} + \frac{1}{\mathrm{Re}} \partial_j \partial_j \hat{u}_m + i k_j \hat{\tau}^{\perp}_{mj} + \mathcal{O}(\varepsilon) \tag{14}$$

where $\hat{h}^{\perp}_{ij} = \left(\delta_{im} - \frac{k_i k_m}{k_l k_l} \right) \hat{h}_{mj}$ and $\hat{\tau}^{\perp}_{ij} = \left(\delta_{im} - \frac{k_i k_m}{k_l k_l} \right) \hat{\tau}_{mj}$.

REFERENCES

del Álamo, J. C. & Jiménez, J. 2003 Spectra of the very large anisotropic scales in turbulent channels. *Phys. Fluids* **15** (6), L41–L44.

Ashurst, W. T., Kerstein, A., Kerr, R. & Gibson, C. 1987 Alignment of vorticity and scalar gradient with strain rate in simulated navier–stokes turbulence. *The Physics of fluids* **30** (8), 2343–2353.

Bae, H. J. 2018 *Investigation of dynamic subgrid-scale and wall models for turbulent boundary layers*. PhD Thesis, Stanford University.

Bae, H. J., Lozano-Duran, A., Bose, S. & Moin, P. 2018 Turbulence intensities in large-eddy simulation of wall-bounded flows. *Physical Review Fluids* **3** (1), 014610.

Balakumar, B. & Adrian, R. 2007 Large-and very-large-scale motions in channel and boundary-layer flows. *Philosophical Transactions of the Royal Society of London A: Mathematical, Physical and Engineering Sciences* **365** (1852), 665–681.

Bassenne, M., Esmaily, M., Livescu, D., Moin, P. & Urzay, J. 2019 A dynamic spectrally enriched subgrid-scale model for preferential concentration in particle-laden turbulence. *International Journal of Multiphase Flow* **116**, 270–280.

Batchelor, G. K. 1953 *The Theory of Homogeneous Turbulence*. Cambridge University Press.

Bose, S. T. & Park, G. I. 2018 Wall-modeled large-eddy simulation for complex turbulent flows. *Annual review of fluid mechanics* **50**, 535–561.

Bou-Zeid, E., Meneveau, C. & Parlange, M. 2005 A scale-dependent lagrangian dynamic model for large eddy simulation of complex turbulent flows. *Phys. Fluids* **17** (2), 025105.

Brasseur, J. G. & Wei, T. 2010 Designing large-eddy simulation of the turbulent boundary layer to capture law-of-the-wall scaling. *Physics of Fluids* **22** (2), 021303.

Cantwell, B. J. 1992 Exact solution of a restricted euler equation for the velocity gradient tensor. *Physics of Fluids A: Fluid Dynamics* **4** (4), 782–793.

Canuto, V. & Dubovikov, M. 1996 A dynamical model for turbulence. I. General formalism. *Phys. Fluids* **8** (2), 571–586.

Carati, D., Ghosal, S. & Moin, P. 1995 On the representation of backscatter in dynamic localization models. *Physics of Fluids* **7** (3), 606–616.

Deardorff, J. W. 1970 A three-dimensional numerical investigation of the idealized planetary boundary layer. *Geo. and Astro. Fluid Dyn.* **1** (3-4), 377–410.

Debnath, L. & Shah, F. A. 2002 *Wavelet transforms and their applications*. Springer.

Doan, N. A. K., Swaminathan, N., Davidson, P. & Tanahashi, M. 2018 Scale locality of the energy cascade using real space quantities. *Physical Review Fluids* **3** (8), 084601.

Dubrulle, B., Laval, J.-P., Nazarenko, S. & Kevlahan, N.-R. 2001 A dynamic subfilter-scale model for plane parallel flows. *Physics of Fluids* **13** (7), 2045–2064.

Dubrulle, B., Laval, J.-P., Sullivan, P. P. & Werne, J. 2002 A new dynamical subgrid model for the planetary surface layer. part i: The model and a priori tests. *Journal of the atmospheric sciences* **59** (4), 861–876.

Farge, M. & Schneider, K. 2001 Coherent vortex simulation (cvs), a semi-deterministic turbulence model using wavelets. *Flow, Turbulence and Combustion* **66** (4), 393–426.

Flohr, P. & Vassilicos, J. 2000 A scalar subgrid model with flow structure for large-eddy simulations of scalar variances. *Journal of Fluid Mechanics* **407**, 315–349.

Fung, J. C. H., Hunt, J. C., Malik, N. & Perkins, R. 1992 Kinematic simulation of homogeneous turbulence by unsteady random fourier modes. *Journal of Fluid Mechanics* **236**, 281–318.

Ghate, A., Towne, A. & Lele, S. 2020 Broadband reconstruction of inhomogeneous turbulence using spectral proper orthogonal decomposition and gabor modes. *Journal of Fluid Mechanics* **888**.

Ghate, A. S. 2018 *Gabor Mode Enrichment in Large Eddy Simulation of Turbulent Flows*. PhD Thesis, Stanford University.

Ghate, A. S. & Lele, S. K. 2017 Subfilter-scale enrichment of planetary boundary layer large eddy simulation using discrete fourier–gabor modes. *J. Fluid Mech.* **819**, 494–539.

Goldstein, D. E. & Vasilyev, O. V. 2004 Stochastic coherent adaptive large eddy simulation method. *Physics of Fluids* **16** (7), 2497–2513.

Greengard, L. & Lee, J.-Y. 2004 Accelerating the nonuniform fast fourier transform. *SIAM review* **46** (3), 443–454.

Hamlington, P. E., Schumacher, J. & Dahm, W. J. 2008 Direct assessment of vorticity alignment with local and nonlocal strain rates in turbulent flows. *Physics of Fluids* **20** (11), 111703.

Hutchins, N. & Marusic, I. 2007 Evidence of very long meandering features in the logarithmic region of turbulent boundary layers. *Journal of Fluid Mechanics* **579**, 1–28.

Jiang, Q., Wang, S. & Sullivan, P. 2018 Large-eddy simulation study of log laws in a neutral ekman boundary layer. *Journal of the Atmospheric Sciences* **75** (6), 1873–1889.

Jiménez, J. 2012 Cascades in wall-bounded turbulence. *Ann. Rev. Fluid Mech.* **44**.

Johnson, P. L. 2020 Energy transfer from large to small scales in turbulence by multiscale nonlinear strain and vorticity interactions. *Physical Review Letters* **124** (10), 104501.

Kawai, S. & Asada, K. 2013 Wall-modeled large-eddy simulation of high reynolds number flow around an airfoil near stall condition. *Computers & Fluids* **85**, 105–113.

Kawai, S. & Larsson, J. 2012 Wall-modeling in large eddy simulation: Length scales, grid resolution, and accuracy. *Physics of Fluids* **24** (1), 015105.

Kelly, M. C. 2018 From standard wind measurements to spectral characterization: turbulence length scale and distribution. *Wind Energy Science* **3** (2), 533–543.

Kosović, B. 1997 Subgrid-scale modelling for the large-eddy simulation of high-reynolds-number boundary layers. *Journal of Fluid Mechanics* **336**, 151–182.

Kraichnan, R. H. 1970 Diffusion by a random velocity field. *The physics of fluids* **13** (1), 22–31.

Larsson, J., Kawai, S., Bodart, J. & Bermejo-Moreno, I. 2016 Large eddy simulation with modeled wall-stress: recent progress and future directions. *Mechanical Engineering Reviews* **3** (1), 15–00418.

Laval, J., Dubrulle, B. & Nazarenko, S. 2001 Nonlocality and intermittency in three-dimensional turbulence. *Physics of Fluids* **13** (7), 1995–2012.

Laval, J.-P., Dubrulle, B. & Nazarenko, S. 2004 Fast numerical simulations of 2d turbulence using a dynamic model for subfilter motions. *Journal of Computational Physics* **196** (1), 184–207.

Leonard, A. 1975 Energy cascade in large-eddy simulations of turbulent fluid flows. In *Advances in geophysics*, , vol. 18, pp. 237–248. Elsevier.

Lozano-Durán, A. & Jiménez, J. 2014 Effect of the computational domain on direct simulations of turbulent channels up to $\mathrm{Re}_\tau = 4200$. *Phys. Fluids* **26** (1), 011702.

Lumley, J. L. 1970 *Stochastic tools in turbulence*. Academic Press.

Lund, T. S. & Rogers, M. M. 1994 An improved measure of strain state probability in turbulent flows. *Physics of Fluids* **6** (5), 1838–1847.

Mallat, S. 1999 *A wavelet tour of signal processing*. Elsevier.

Mann, J. 1994 The spatial structure of neutral atmospheric surface-layer turbulence. *Journal of fluid mechanics* **273**, 141–168.

Mazzitelli, I. M., Toschi, F. & Lanotte, A. S. 2014 An accurate and efficient lagrangian sub-grid model. *Physics of Fluids* **26** (9), 095101.

Meneveau, C. & Katz, J. 2000 Scale-invariance and turbulence models for large-eddy simulation. *Ann. Rev. Fluid Mech.* **32** (1), 1–32.

Misra, A. & Pullin, D. I. 1997 A vortex-based subgrid stress model for large-eddy simulation. *Physics of Fluids* **9** (8), 2443–2454.

Moeng, C.-H. 1984 A large-eddy-simulation model for the study of planetary boundary-layer turbulence. *J. of the Atm. Sci.* **41** (13), 2052–2062.

Nazarenko, S., Kevlahan, N.-R. & Dubrulle, B. 1999 Wkb theory for rapid distortion of inhomogeneous turbulence. *Journal of Fluid Mechanics* **390**, 325–348.

Nicoud, F., Toda, H., Cabrit, O., Bose, S. & Lee, J. 2011 Using singular values to build a subgrid-scale model for large eddy simulations. *Phys. Fluids* **23** (8), 085106.

Piomelli, U. & Balaras, E. 2002 Wall-layer models for large-eddy simulations. *Ann. Rev. Fluid Mech.* **34** (1), 349–374.

Porté-Agel, F., Meneveau, C. & Parlange, M. 2000 A scale-dependent dynamic model for large-eddy simulation: application to a neutral atmospheric boundary layer. *J. Fluid Mech.* **415**, 261–284.

Pullin, D. & Saffman, P. 1994 Reynolds stresses and one-dimensional spectra for a vortex model of homogeneous anisotropic turbulence. *Physics of Fluids* **6** (5), 1787–1796.

Pullin, D. & Saffman, P. 1998 Vortex dynamics in turbulence. *Annual review of fluid mechanics* **30** (1), 31–51.

Rozema, W., Bae, H. J., Moin, P. & Verstappen, R. 2015 Minimum-dissipation models for large-eddy simulation. *Physics of Fluids* **27** (8), 085107.

Schneider, K. & Vasilyev, O. V. 2010 Wavelet methods in computational fluid dynamics. *Annual Review of Fluid Mechanics* **42**.

Schumann, U. 1975 Subgrid scale model for finite difference simulations of turbulent flows in plane channels and annuli. *Journal of computational physics* **18** (4), 376–404.

She, Z.-S., Jackson, E. & Orszag, S. A. 1990 Intermittent vortex structures in homogeneous isotropic turbulence. *Nature* **344** (6263), 226.

Smits, A. J., McKeon, B. J. & Marusic, I. 2011 High–reynolds number wall turbulence. *Ann. Rev. Fluid Mech.* **43**, 353–375.

Spalart, P. R. 2015 Philosophies and fallacies in turbulence modeling. *Progress in Aerospace Sciences* **74**, 1–15.

Spyropoulos, E. T. & Blaisdell, G. A. 1996 Evaluation of the dynamic model for simulations of compressible decaying isotropic turbulence. *AIAA journal* **34** (5), 990–998.

Stevens, R. J., Wilczek, M. & Meneveau, C. 2014 Large-eddy simulation study of the logarithmic law for second-and higher-order moments in turbulent wall-bounded flow. *Journal of fluid mechanics* **757**, 888–907.

Sullivan, P. P. & Patton, E. G. 2011 The effect of mesh resolution on convective boundary layer statistics and structures generated by large-eddy simulation. *Journal of the Atmospheric Sciences* **68** (10), 2395–2415.

Tomkins, C. D. & Adrian, R. J. 2003 Spanwise structure and scale growth in turbulent boundary layers. *J. Fluid Mech.* **490**, 37–74.

Townsend, A. 1951 On the fine-scale structure of turbulence. *Proceedings of the Royal Society of London. Series A. Mathematical and Physical Sciences* **208** (1095), 534–542.

Wyngaard, J. C. 2010 *Turbulence in the Atmosphere*. Cambridge University Press.

Xiong, Z., Nagarajan, S. & Lele, S. K. 2004 Simple method for generating inflow turbulence. *AIAA journal* **42** (10), 2164–2166.

Yang, X. I., Park, G. I. & Moin, P. 2017 Log-layer mismatch and modeling of the fluctuating wall stress in wall-modeled large-eddy simulations. *Physical Review Fluids* **2** (10), 104601.